Department of Physics and Astronomy
University of Heidelberg

Master thesis
in Physics
submitted by

Dennis Sauter

born in Speyer

December 2018

MRPC Prototype 3a & 3b performance studies at the cosmic radiation test setup of the CBM-TOF group in Heidelberg

This Master thesis has been carried out by Dennis Sauter at the
Physikalisches Institut in Heidelberg
under the supervision of
Prof. Dr. N. Herrmann

Abstract

Ziel dieser Arbeit war es, die für die Nutzung in CBM TOF geplanten Detektorprototypen MRPC 3a & 3b zu testen. Es ist geplant, diese Typen in dem Teil der TOF-Wand zu verwenden, für den niedrige bis mittlere Teilchenraten erwartet werden. Dieser Test bediente sich kosmischer Myonenstrahlung zur Bestimmung der Leistungsfähigkeit der Detektoren. Zur Analyse stand erstmals ein Tracking-Algorithmus zur Teilchenbahnrekonstruktion zur Verfügung. Der Aufbau bestand aus 6 Detektorlagen, die im Mittel eine Zeitauflösung von ungefähr 50 ps bei einer Effizienz von über 95 % vorweisen konnten. Zusätzlich war es dadurch möglich, Winkelabhängigkeiten in der Messung zu erkennen und aufzuzeigen. Darüber hinaus konnten in seltenen Fällen auch Teilchenbahnen gefunden werden, die den Aufbau von unten nach oben durchquerten. Die anfängliche Vermutung, dass es sich um seltene, durch Neutrinos verursachte, Myon-Ereignisse handelt wurde widerlegt. Stattdessen konnten diese schließlich als Elektronen, resultierend aus Myon-Zerfällen, identifiziert werden. In kommenden Strahlzeiten wie etwa dem mCBM-Experiment im Jahr 2019 soll ermittelt werden, ob die bis dato zufriedenstellende Performance der Detektoren auch unter experimentnahen Raten gehalten werden kann.

This thesis contains the performance testing of CBM TOF's detector type MRPC 3a & 3b using cosmic muons. These detectors are planned to be used in the CBM experiment as part of the intermediate and low rate region of the wall. Unlike previous studies, this was performed by using an actual tracker for particle track reconstruction based on a stack of 6 stations. The results show that both types have the required accuracy in time measurement of about 50 ps at efficiencies of over 95 %. With the advantage of tracking it was furthermore possible to do angular based research with both, azimuthal and polar, angles. In addition, signals of particles that seemed to come from below the setup were found. The first assumption of neutrino induced muon interactions was proven wrong and instead electrons from muon decays were held responsible for this phenomenon. For low rate cosmic muon events, the detectors proved working as desired. The upcoming mCBM beamtime at GSI will give insight whether this can be kept at the required rates or even above.

Contents

Chapter 1

Introduction

1.1 CBM Experiment

The CBM[1] experiment is a future project at FAIR[2] to test strongly interacting matter at high net-baryon densities in the SIS-100 collider. With high interaction rates of fixed target gold-on-gold collision the properties of baryonic matter and the transition to the quark-gluon plasma are planned to be studied. To achieve this, exceptionally accurate particle identification is needed. Therefore an interplay of various detectorsystems to ensure unambiguous identification, even at high particle momenta with beam energies up to 11 AGeV and center-of-mass energies of 4-5 GeV per nucleon, is aimed at.
The CBM detectorsystem includes a large set of different detector types. Each is specialized in one task. As a whole ensemble, this leads to remarkable particle identification capabilities even at an interaction rate of 10 MHz. In one of several strategies to measure the event start time, directly in front of the gold-target sits a diamond T_0 detector that accurately measures the passing time of the gold ions in the beam. Together with the time information of the roughly 10 m distant TOF[3]system, the eponymous time of flight can be measured to high precision. Together with the distance, which the particle travelled, the velocity can be determined accurately. In combination with the particles mo-

[1] Compressed Baryonic Matter [2] Facility for Antiproton and Ion Research
[3] Time-of-Flight

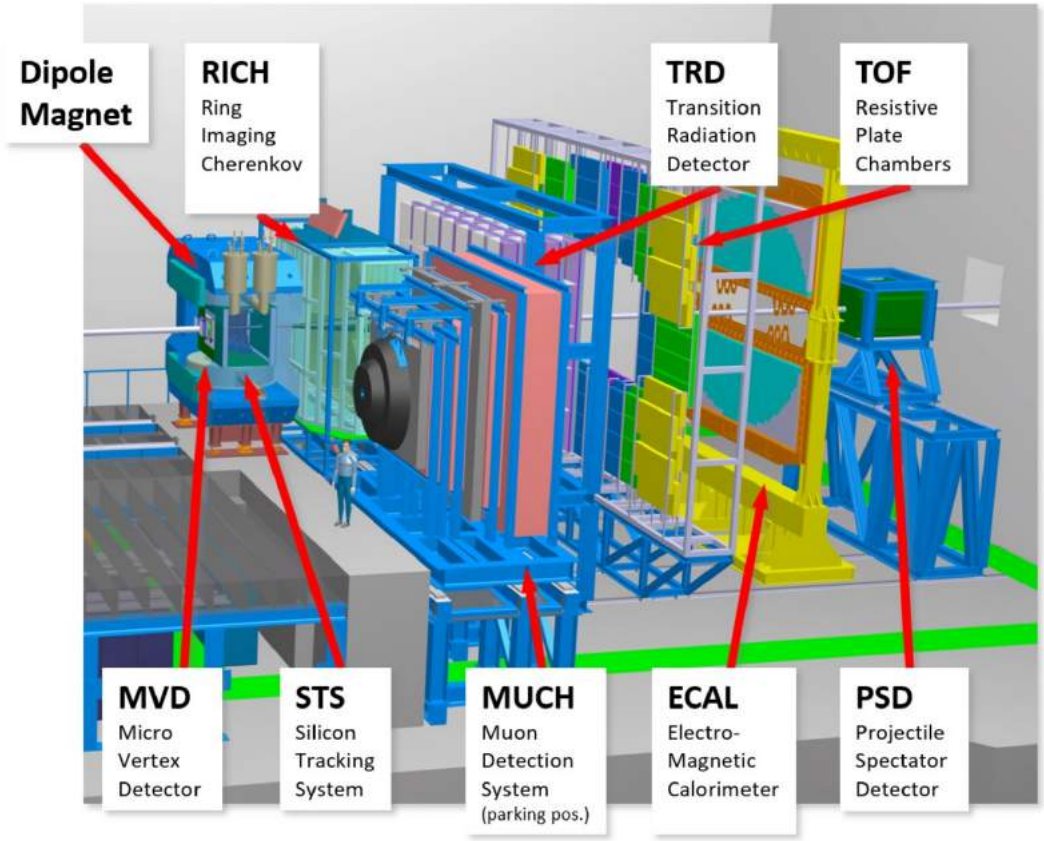

Figure 1.1: Construction plan of the CBM detector system.
The gold beam enters from the left and hits the target right in front of the MVD. The extensive amount of produced particles then travels to the right through all the detector subsystems to be precisely measured. Taken from [1].

mentum, the mass can be calculated, which uniquely defines the particle species. Said momentum measurement will be done by the STS[4] station that sits inside a large dipole magnet. Through precise spatial tracking, the curvature of the trajectory inside the magnetic field provides information about the particles momentum. Further improvements in precision require more stations that can be included in the track reconstruction. This is one of the tasks of the TRD[5] that stands in front of TOF. With its three layered structure it provides additional information to work with for the track building process. The other

[4] Silicon Tracking System [5] Transition Radiation Detector

task is measuring a lower limit of the Lorentz factor γ of passing particles to further enhance particle identification capabilities. With this whole time of flight approach it is achievable to separate protons from kaons and kaons from pions. Shortly behind the target, the MVD[6] is positioned, which is the detector closest to the collision. Secondary vertices from heavier short lived hadrons containing strange, charm and bottom quarks can be resolved in this system to identify the decaying particle. The lower end of the mass spectrum like pions, electrons and muons cannot be separated using the time of flight approach. They essentially all come at the speed of light for the given collision energy. The task to separate them was assigned to MUCH[7], RICH[8], ECAL[9] and also the TRD. These systems are especially designed for charged lepton identification. All systems together cover the majority of possible interaction products and should be highly efficient in reconstruction of most of the events. Lastly there is also the PSD[10], responsible for determining the centrality of the collision by looking at the spectators, i.e. the non-interacting part of the colliding nuclei.
In the following it is roughly explained what the CBM experiment is trying to accomplish.

1.2 QCD Theory

The motivation behind heavy-ion physics experiments and the research of QCD[11], i.e. the effective field theory of the strong interaction, is its complexity and the difficulty to make theoretical predictions. The coupling strength of QCD is of the order of 1 and as such, perturbation theory is not applicable. Only computationally expensive approximations through lattice theories are possible. Though these require super-computers from all over the world. Unlike QED[12], QCD is a non-abelian field theory, meaning the gauge boson itself carries the associated charge. One of the consequences of this is the so-called *confinement* of colour. The self-interaction of the gluon leads to an increase in

[6] Micro Vertex Detector [7] Muon Chambers [8] Ring Imaging Cherenkov [9] Electromagnetic Calorimeter [10] Projectile Spectator Detector [11] Quantum Chromodynamics [12] Quantum Electrodynamics

field-energy, the further one tries to separate quarks. At roughly 1 fm distance, enough energy is stored in the gluonic field to produce a new pair of quarks. As a result, only colour neutral "white" states, such as bosonic mesons ($q\bar{q}$) and fermionic baryons (qqq or $\bar{q}\bar{q}\bar{q}$) are viable and no free quarks can exist in hadronic matter. As another consequence of self interacting gluons, the coupling strength decreases with increasing energies, i.e. on smaller distance scales. At energies above a few 10's of GeV, the coupling is weak enough to allow for perturbation theory calculations. This decrease in the running coupling is called *asymptotic freedom* of QCD. Another defining characteristic of QCD would be the spontaneously broken chiral symmetry. Chiral symmetry applies to massless particles for which helicity and chirality coincides. Consider massless up- and down-quarks as their mass is low compared to the QCD scale of $\sim$200 MeV. The underlying group symmetry states a $SU(2)_L \times SU(2)_R$ symmetry for the left-handed and right-handed chiral states. The quark condensate $\langle 0 \mid q\,\bar{q} \mid 0 \rangle$ or QCD vacuum fluctuation breaks this symmetry, resulting in 3 massless Nambu-Goldstone bosons. These 3 bosons can be identified as $\pi^{\pm}$ and π^0. However, neither the up-quark nor the down-quark are massless in reality, so the pions end up massive, too. Similar to the Higgs mechanism this gives rise to an additional mass term. Adding up all the bare quark masses inside a proton only reproduces 1 % of its mass. In fact, almost all of the mass of the matter surrounding us everyday stems from chiral symmetry breaking rather than the Higgs mechanism. Adding the strange quark to the ranks of light quarks increases the chiral symmetry to an $SU(3)_L \times SU(3)_R$. After the symmetry is broken one obtains 8 Goldstone bosons as force carriers. These are the three pions $\pi^{\pm}$ and π^0, four kaons $K^{\pm}$, K^0 and $\bar{K}^0$ and the eta meson η. The QCD phase diagram is a theoretical construct, that yet has to be researched in full detail through experiments. The thermodynamic variables of strongly interacting matter are temperature and pressure. The latter can be transformed to be represented by the baryon chemical potential, a measure of the net baryon density. While colliders like the LHC follow the path of vanishing baryon chemical potential and extremely high temperatures, heavy ion collision experiments like CBM plan to investigate the behaviour at mod-

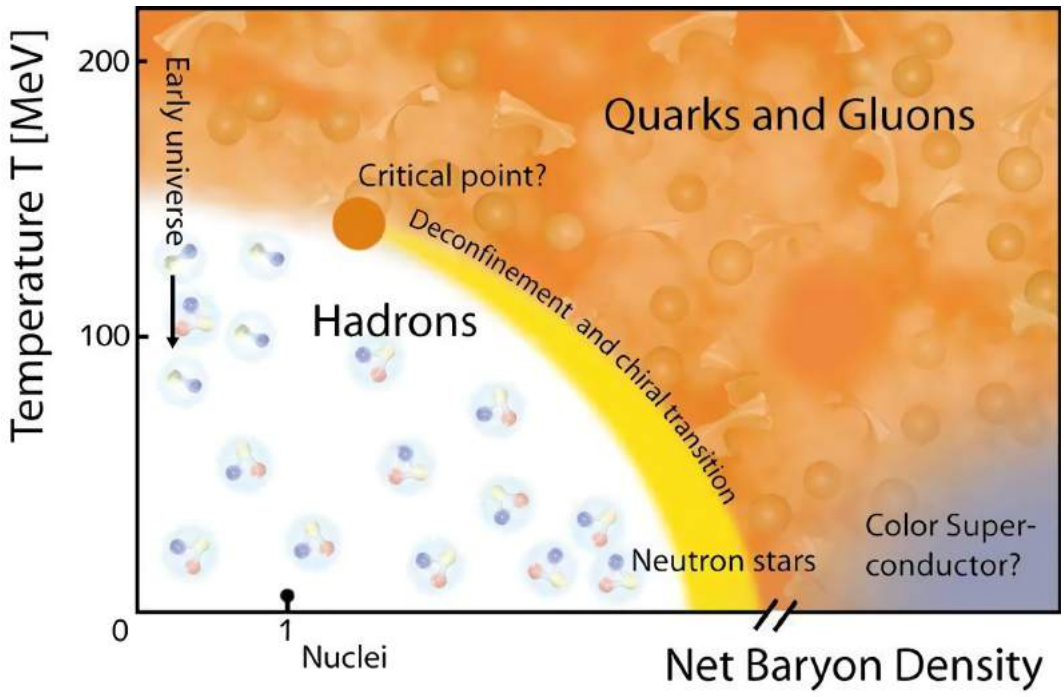

Figure 1.2: A sketch of the phase diagram of strongly interacting matter. Most of the features shown are only theoretical predictions and need yet to be confirmed or refuted. What CBM strives for is the phase transition region positioned in the center of the shown diagram. It is characterized by moderate temperatures (relative to other colliders) and high baryon densities.

erate temperatures and high baryon densities. In this region, one expects a transition from the hadron gas phase to the quark gluon plasma. Subject of current research is the search for evidence of a first or second order phase transition. According to our current knowledge there might be not only one transition but two. A transition where the spontaneously broken chiral symmetry is restored as well as a transition into deconfined quark matter. Deconfinement refers to a melting of the hadrons. Through high temperatures and/or densities, the overlap between hadrons increases. As a result, the hadrons are not separable anymore and the boundaries disappear. This state of quark matter is called QGP [13] as the quarks inside are not bound to hadrons but move freely within. In contrast to the electromagnetic gas-like plasma, the QGP behaves

[13] Quark-gluon plasma

like an ideal Fermi liquid because of the strong interaction's great strength. The hydrodynamics of such a liquid makes it experimentally accessible and possible to identify it as such.
The strangeness production in a QGP is enhanced and usually rare multi-strange hadrons appear more often. The formation of strangeness containing baryons during freeze-out is typically observed after formation of a QGP. The time-of-flight approach is targeting the remnants of these rare products to probe the transition into deconfined matter.
On the other hand, the restoration of chiral symmetry is identified by the produced mesons' mass. In the chiral limit the mass difference of the ρ vector meson and the a_1 pseudo vector meson, originating from chiral symmetry breaking, vanishes. At the end of their decay chain, most of the mesons end up as pairs of leptons. These di-leptons are measured in the MUCH, RICH, ECAL and TRD to determine the parent particles mass. The high rates are needed to gain sufficient statistics even for rarely produced particles.
The following thesis contains analysis results from the TOF test setup in Heidelberg. First, an introduction to the used detector type is provided in chapter 2. Chapter 3 mainly explains how the test setup in Heidelberg looks like and how the hardware is arranged. After that a brief review about the analysis software and the required calibration steps is given in chapter 4. Shortly after, in chapter 5, the main part of this thesis is presented in the form of analysis results. Chapter 6 contains a short summary of the results and a future outlook based on them.

Chapter 2

Resistive Plate Chamber

One of the aforementioned CBM sub systems is TOF, which has the task to measure precisely the flight time and therefore the velocity of traversing particles. This is done with a $120\,\mathrm{m}^2$ large wall roughly 10 meters away from the target. It is consisting out of MRPCs[1] with efficiencies close to 100 % and time resolutions down to 50 ps. The structure of RPCs in its core is a large plate capacitor with high electric fields inside. When a particle traverses such a capacitor, it ionizes the gas on its way through the active volume. The resulting negatively charged electrons and positively charged ions get accelerated due to the field until enough energy is accumulated to ionize further atoms of the gas. Since the ions are much more inert compared to the electrons, because of their orders of magnitude larger mass, the ionic contribution becomes neglectable. The exponential growth in free electrons will at some point reach the positively charged plate of the capacitor and leave a plasma tunnel behind. Through this conductive tube it is now possible for the capacitor to discharge with a spark, which is detectable. Up to this point this describes the work principles of a spark chamber. The big disadvantage however is the rather long charging time that is needed to rebuild the electric field. For high rate purposes this is a severe problem. An advance in this type of detector is the development of the RPC, which includes an additional resistive plate in between the capacitor plates, which gives the detector its name. Here, resistive is

[1] Multigap Resistive Plate Chamber

referring to a material that barely conducts electricity but is not an insulator. This feature is important, as it allows the plate to catch the growing avalanche of the initial ionization and transports the charge out of the detector. In this way, one prevents the full discharge of the capacitor because no plasma tunnel connects both high voltage electrodes. A further improvement in performance is reached through adding multiple of such plates, therefore it is called MRPC. Through this, one gets multiple small gaps where ionization can happen while minimizing the challenge of recharging the electrodes. Now, one has to find a way to acquire a signal from these multiple avalanches inside. One way to achieve this is the usage of readout strips. These metal strips sit outside of the capacitor right after the high voltage electrodes. They function with the principle of induction. Since the avalanches inside the gaps are essentially highly accelerated charged particles, they will induce a small voltage on these readout strips. Figure 2.1 shows the described structure in a schematic illustration. Another minor challenge is the possibility to acquire signals with the readout strips. Owing to the construction, the strips are shielded by the high voltage electrodes that are not transparent to high frequency signals if made out of metal. A compromise between transparency for high frequency signals and a fast enough recharge potential is therefore desirable when choosing the resistivity of the high voltage electrodes. Additionally one can construct an MRPC in a symmetric or an antisymmetric way. The latter does only have two high voltage electrodes charged positively and negatively. The symmetric construction has three electrodes that are charged alternately. The antisymmetric one is called singles-stack and the other likewise double-stack, since it is essentially two single-stacks. An advantage of the double-stack is the need of only half of the high voltage to operate with same field strengths. Depending on the used power supply this may come in handy. The single-stack has an theoretical advantage over the double stack design. The initial particle moves in a boosted frame relative to the lab and so does the electron that gets kicked out. Facing the correct way, the electric field accelerates the electron further which should in principle speed up the avalanche formation. In the double-stack, avalanche formation is slowed down in one half and accelerated in the

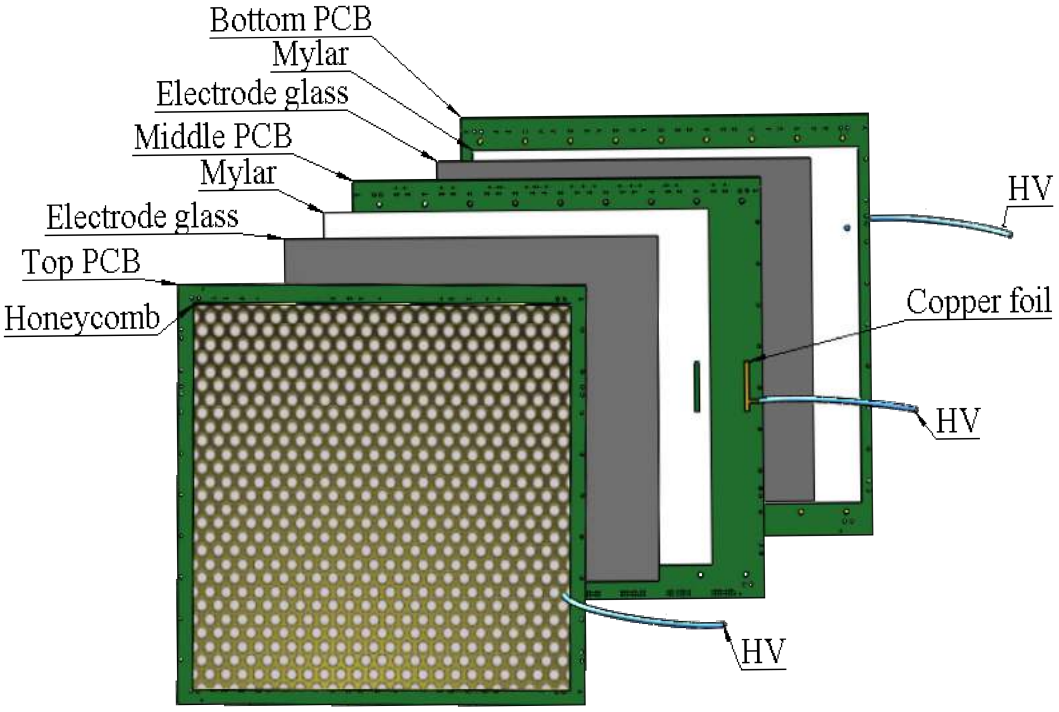

Figure 2.1: Explosive view schematic of the structure of an double stack MRPC.
Three PCBs, covered with readout strips, are isolated from the HV electrodes.For the sake of simplicity and clarity only one glass plate in each stack is drawn. The honeycomb structure on the outside increases mechanical stability with minimal further material gain. Taken and modified from [2]

other half of the detector. This potentially smears out the timing and leads to worse resolutions. Research in this regard, comparing both designs, showed no measurable difference.

Typical operational fields are in the order of 100 kV/cm. This exceeds the dielectric strength of regular air by far. Depending on the air's humidity, it breaks down at only 1/10 th of the needed voltage. That is the reason why one has to put the detectors in boxes and flood them with a special composition of gases. These gases have to satisfy mainly three conditions. As mentioned before, first of all a high dielectric strength is a strong requirement. Second is

a high electronegativity to prevent the avalanche from too rapid growth and to reduce noise by catching free electrons. Accelerated and decelerated electrons will emit secondary photons, which in turn can create secondary avalanches, called streamers. Streamers are essentially bad for accurately measuring the arrival time and the location of a particle and one has to take care of them. The third requirement is the ability to absorb these photons sufficiently fast. High electronegative gases are usually those, that contain fluorine in some form. Fluorine is the most electronegative element in the periodic table and is very efficient in binding free electrons. For our gas composition, mainly 1,1,1,2-Tetrafluoroethane ($C_2H_2F_4$) and Sulfur hexafluoride (SF_6) are used for this task.

Photon absorption is maintained by larger molecules. Those usually have many degrees of freedoms for state excitations. Suitable are therefore hydrocarbons, which can form molecules of any length and complexity. In our case the choice fell on Isobutane (C_4H_{10}) as only a few percent of concentration is enough to quench photons sufficiently.

One distinguishes between two operating modes of MRPC's. In the so-called streamer mode no streamer suppressing gas is used and a high voltage favors the development of streamers. The sole purpose of the MRPC is delivering a trigger signal for the rest of the detectors as time precision suffers heavily with streamers. On the other hand, Time-of-Flight based applications use them in the so-called avalanche mode. This is ensured by only applying moderate high-voltage, predetermined through testing, and the usage of photon-quenching gas to suppress streamers. In this mode the timing information is comparably superior and allows for precise Time-of-Flight measurements with 10's of ps in precision.

Chapter 3

Experimental Test Setup

The TOF wall is divided in various regions depending on their estimated irradiation rate. In the inner region close to the beam one uses ceramics as resistive material whereas the outer regions use soda-lime float glass and low resistive glass as material. Amongst others, the University of Heidelberg houses a cosmic test stand for the CBM TOF group where muons are measured in a stack of MRPCs to study their properties. The tested detectors in Heidelberg are of the type MRPC3a & MRPC3b, build with low resistive glass and float glass respectively. In Figure 3.1 you can see a prototype of MRPC3a (3.1a), which is produced in the Tsinghua University in China on the left hand side while on the right hand side a prototype of MRPC3b (3.1b) is shown that was produced in USTC[1] in China.
As shown in Table 3.1, the detectors differ in the type of glass they use as well as the thickness of the glass. The MRPC3b has in addition one more gas gap per stack to counter the smaller gap size compared to the MRPC3a. A difference, which only concerns the polarity of the readout electronics is the exchange of positive and negative high voltage polarity relative to each other.

[1] University of Science & Technology of China

(a) (b)

Figure 3.1: Topview and sideview of the glass inside the MRPC3a (a) and MRPC3b (b). The glass on the left is low resistive glass and due to atom injections during the production coloured black. On the right, regular float glass is used. It is polished down to almost 1/3 the thickness than on the left side.

	MRPC3a	**MRPC3b**
MRPC type	double stack	double stack
High voltage polarity	$+-+$	$-+-$
electrode material	low resistive glass	soda-lime glass
glass thickness	700 μm	280 μm
gas gap number	8	10
gas gap size	250 μm	230 μm
readout strip number	32	32
strip length	27 cm	27 cm
strip width	0.7 cm	0.7 cm
strip pitch	1 cm	1 cm

Table 3.1: Comparison of both MRPC types in their mechanical construction

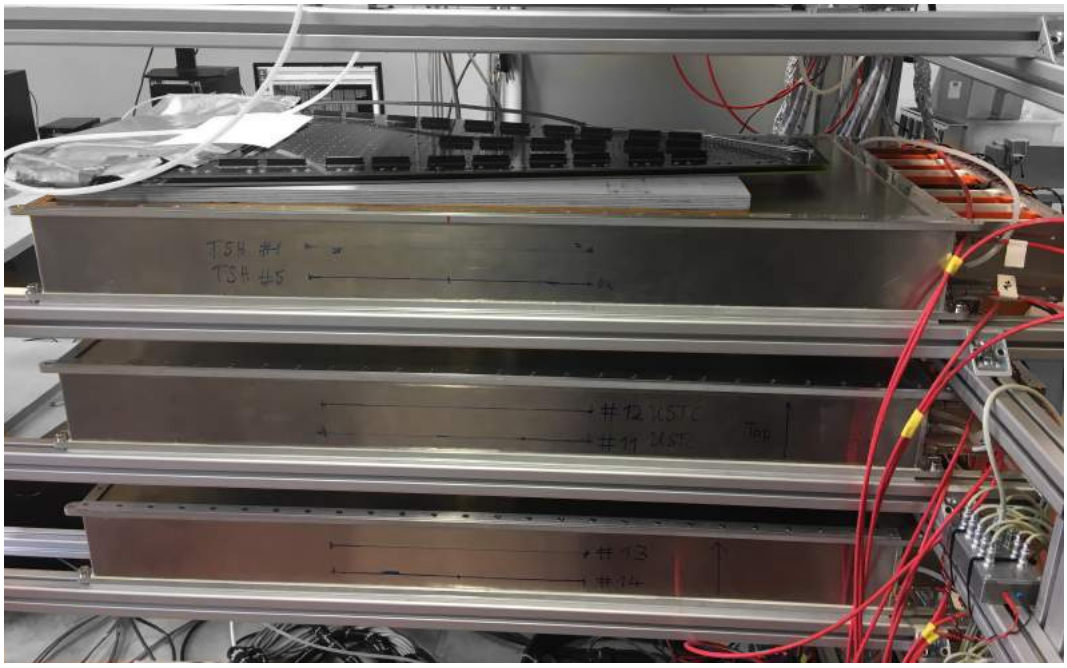

Figure 3.2: A photo of the 3 aluminum boxes, horizontally mounted on a frame to measure cosmic muon radiation. Each box houses 2 MRPCs on top of each other. The interface is on the right side where the electronics is located. High voltage cables (red), low voltage cables to power the electronics, clock distribution and gas pipes are required to operate. Copper data cables are connected to an AFCK for further processing.

The Heidelberg test setup, shown in Figure 3.2, comprises of 3 Modules with each having 2 detectors inside that are mounted on top of each other. The commonly used coordinate frame for TOF puts the detectors in the x-y-plane, such that the incoming beam is pointing towards the z-axis. The y-axis is then pointing along the readout strips and the x-axis points across the strips. This results in a stack with 6 detector layers along the z-axis that can be used for particle tracking and efficiency determination. Directly attached to the MRPCs inside is a PADI[2] to convert the MRPC pulse in a digital signal. The threshold for the digitalisation can be set from outside through an SPI[3] up to -600 mV. A possible impact on detector efficiencies depending on the threshold was measured with several settings and will be shown later in this

[2] Pre Amplifier & Discriminator [3] Serial Peripheral Interface

thesis. This signals are then carried to the backside of the module to the Get4 card (right end on the picture). The Get4 is a TDC[4], which then measures the arrival time with a signal delay chain to determine it with high precision in the order of ps. In addition, the ToT[5] of the signal is measured as well. The ToT is determined by calculating the difference between leading edge and trailing edge of the digital signal. It is a measure of the amplitude of the amplified original signal before digitalization and therefore representative for the charge deposition of the avalanche. Figure 3.3 illustrates how one derives these quantities. The black analogous signal is the amplified signal of the MRPC. The discriminator is working based on a adjustable threshold, here shown in red. Whenever the signal crosses the threshold, the digital signal flips its sign and therefore creates a pulse. This digital pulse, here the blue line, can then be processed by the subsequent electronics. ToT is calculated by taking the difference $\mathbf{t}_2 - \mathbf{t}_1$ and $\mathbf{t}_1$ is treated as the signals arrival time.

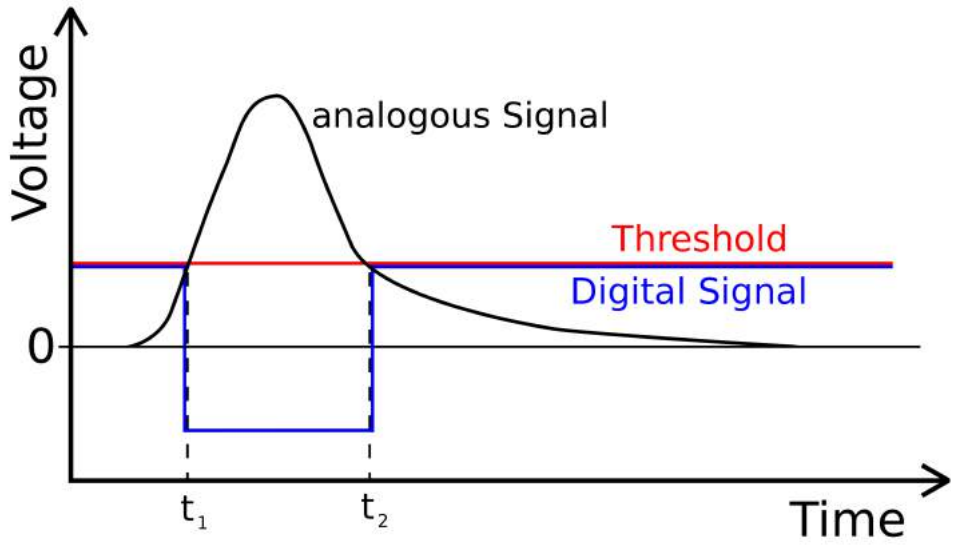

Figure 3.3: Principle of operation of the discriminator. The time scale is in the order of ns and the voltage scale is usually on the millivolt level. The arrival time is $\mathbf{t}_1$ and the ToT is $\mathbf{t}_2 - \mathbf{t}_1$.

[4] Time-to-Digital Converter [5] Time over Threshold

The Get4 is located in the electronics housing that is mounted on the interface side of the module's aluminium frame. From here on, the Get4 output then goes via copper cables to an externally mounted AFCK[6] board that is building time slices, which contain the data of all attached Get4. These time slices are subsequently sent via optical fibre to a FLIB[7], a board that is connected to a server computer in the laboratory via PCIe expansion slot. On this FLES[8] called entry node, the data of potentially multiple AFCKs is sorted and written on the hard drive disks. This data acquisition mode is free-streaming and hence no trigger needs to be applied. For a more detailed and in depth description of the DAQ it is recommended to take a look in the CBM Progress Report [1].

[6] AMC FMC Carrier Kintex [7] FLES Interface Board [8] First Level Event Selector

Chapter 4

Analysis software

The Software utilizes the *cbmroot* framework based on *fairroot*. The raw data files are so-called time slice archive files (.tsa) that first need to be unpacked. Since the following analysis uses an event based algorithm, the unpacker creates such events based on specifiable conditions. All analysis done in this thesis used the condition of at least 4 detectors giving a signal in a 50 ns long event-time window. This makes sure that the unpacked data originates from real particles traversing the stack, not from random noise in the detector and electronics, as coincidental signals are requested. Another necessity is the existence of a signal on each side of the same strip, which further excludes noise from the electronics. In this state one refers to the datapoints as digis. A digi consists of an address, which is assigned through mapping files to the specific side of a strip of a certain MRPC, and timing information regarding the arrival time and ToT of the signal. Due to cable routing and therefore length differences and other hardware related contributions, systematic time shifts occur that need to be corrected.
Hence, the next task is a suitable calibration that is done with the *Clusterizer*. The cbmroot class that is handling the clusterization is *CbmTofCosmicClusterizer*. The clusterization method, that is provided by the framework, takes digis and builds so-called hits by assigning them to a space-time point. This is done by taking the arrival time as time-coordinate, the strip number as x-coordinate and the time difference of both strip sides multiplied with the signal velocity

as y-coordinate. During this step, one searches for correlations in the hits of each detector. If two or more digis came close in time and space, it is highly likely that the same avalanche induced a signal on two or more adjacent strips and as a consequence the digis are merged to a single cluster with an integer cluster size referring to the number of strips participating. These clusters then need further calibration such as the following:

1. walk correction:

A larger signal typically takes less time to reach the threshold of the discriminator as its slope is steeper. This has to be accounted for by taking the difference of the arrival time with a defined reference time and plot it against the hit's ToT. On a logarithmic scale one clearly sees a correlation between both quantities as shown in the upper histogram of Figure 4.1. The mean of every ToT bin then gets shifted to the same reference time, here zero, for calibrating out walk contributions. A calibrated walk histogram is then shown in the lower histogram of Figure 4.1 where the red area that includes most of the statistics is essentially flattened. Through this procedure one improves the time resolution by ∼10 ps.

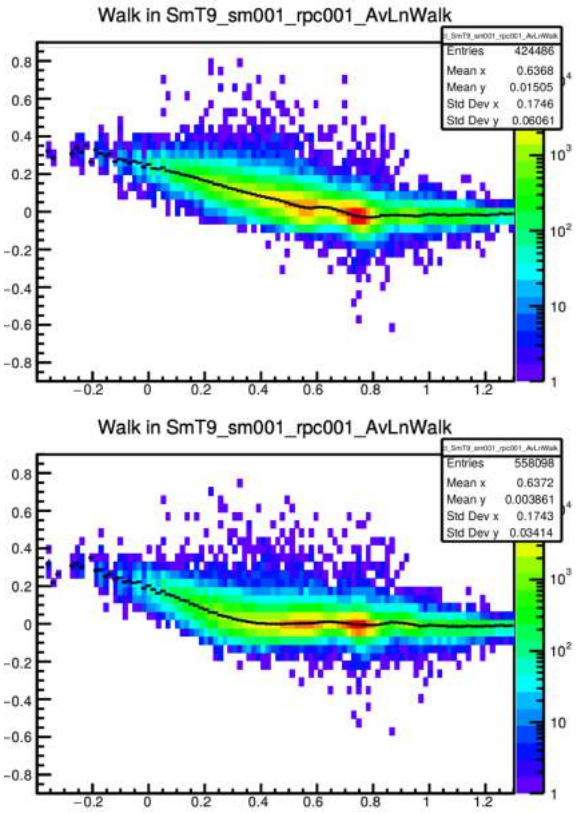

Figure 4.1: The x-axis reads the hit's ToT in a logarithmic scale. The y-axis meanwhile shows the difference of the hits' arrival times relative to a defined reference time in ns. The upper histogram is before walk correction and the lower histogram after applying walk correction. The highly populated area is flat afterwards.

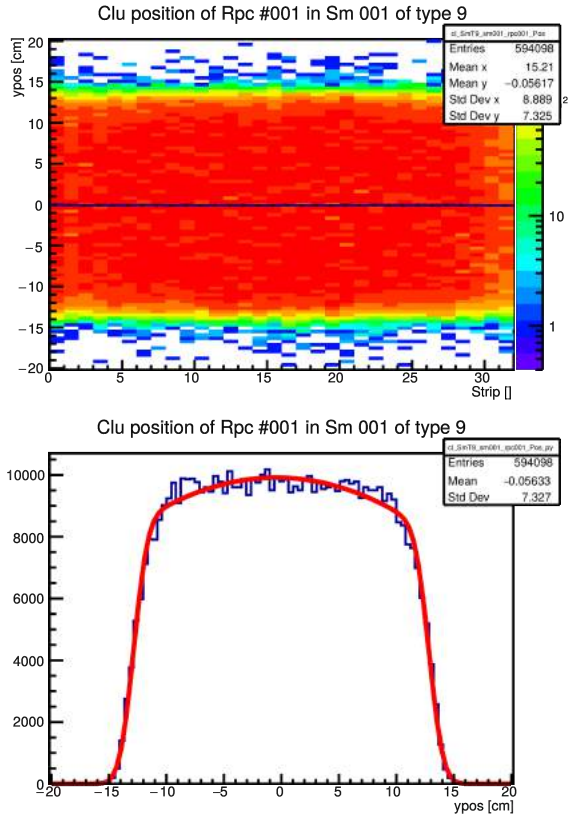

Figure 4.2: Hit distribution over the full detector after calibration. In the upper histogram one recognizes the active area of the MRPC coloured red. The lower histogram is a projection on Y and yields the distribution along the strips. Angular restrictions and finite time resolution lead to slopes instead of sharp edges.

2. position calibration:

The exposure of cosmic radiation is homogeneously distributed over the surface and such should the hit distribution in the x-y-plane of every detector. Minimal differences in cable lengths however cause time shifts of the signals relative to each other that need to be considered. To counter this, for every strip the mean value is determined and shifted towards zero as shown in the upper plot of Figure 4.2. Furthermore it is necessary to calibrate the propagation velocity of the induced signal along the strips. This is done by fitting a box-shaped function over the projection on y (Figure 4.2, below). The width of this box should coincide with the strip length of 27 cm. An underestimation of the signal velocity leads to a longer strip whereas an overestimation of the velocity causes too short strips. The velocity is therefore obtained through strip length and timing. A realistic estimation of the purely electronics time resolution of about 20 ps leads to an accuracy in the velocity of $\sim$1 %. Typical values for the detectors under test range from 16 - 18 cm/ns, which is roughly 1/2 - 1/3 the speed of light. This also sets the limit of our y-resolution to $\sim$1 %, equivalent to 2 - 3 mm.

3. ToT calibration:

The pre amplifier is by no means linear in the amplification of the incoming signal also shows variation with respect to other channels. This leaves one then with a distribution of ToT's per channel that cannot be compared to each other. To properly calibrate these distribution, every channel's ToT gets multiplied by a factor such, that the channel's mean is shifted towards an arbitrary number. In this case it is set to 5 as shown in Figure 4.3. Through this one loses the information about the original ToT since the units are now not ns any more but arbitrary units by stretching the initial scale with this factor. However, to get an estimation of the real ToT values a second axis is rescaled by averaging the factors of all channels. After this calibration procedure is done, the actual performance testing can be started. The method that is at the moment in use of doing so, utilizes the tracking algorithm developed at the physical institute in Heidelberg. The corresponding cbmroot class is called *CbmTofFindTracks*. Through tracking one obtains efficiencies for all detectors as well as time and space resolutions. These characteristics are global but with enough statistics, each detector can be divided to show them in a differential way for certain space cells. The tracking class is determined by a few parameters that describe what it is doing. Most importantly one has to define a χ^2 limit that tells the algorithm how close in space and time a hit has to be at least to a reconstructed track to be accepted as

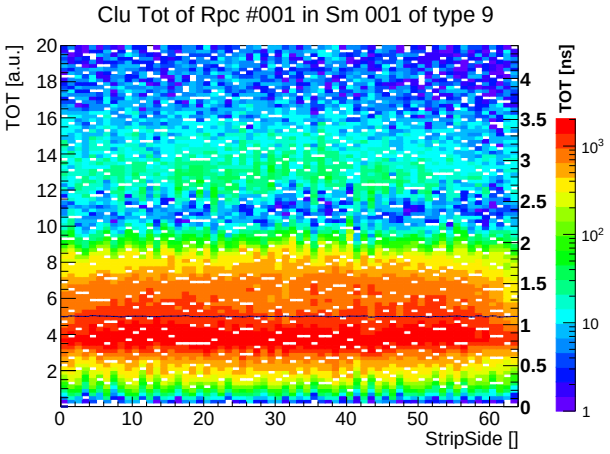

Figure 4.3: ToT distribution for each strip side in one detector. To account for different gains in amplification, the means are shifted to 5. The scale on the right side converts this back to ns with an average around 1,1 ns

part of this track. Increasing the χ^2 limit leads of course to improvements in efficiency as more of the hits are then accepted. On the other hand, however, the spatial and temporal resolutions suffer, due to larger allowed distances to the track. If the χ^2 limit is too high, then one inevitably builds tracks with hits that didn't originate from the same particle.
For tracking to work, it is required to provide the software with information about the physical locations of the detectors relative to each other. The necessary geometry file is created by a Create_TOF_Geometry macro upon inserting the proper distances as parameters. The geometry used for the setup of 6 stacked detectors is version *v18d*. To reconstruct a track the first two detectors are checked for hits and every pair combination of hits builds a tracklet-seed. All other detectors in the stack are then checked if they have an extrapolated or interpolated hit on this tracklet-seed. What determines which detector is the first, second and so on is the *tracking setup* that needs to be defined. This setup contains the number of detectors participating as well as the minimum number of participating detectors to accept the track. Furthermore it is defined in which order the detectors (stations) are checked for matching hits. Experience shows that the first two stations should be the outermost detectors as interpolating errors are far smaller than extrapolation to outer stations. To calculate the efficiency for a given detector, it is counted how many tracks have a matched hit in this detector and how many don't. The formula for the efficiency in our case[1] for detector i is then

$$\epsilon[i] = \frac{\text{\#6-detector tracks}}{\text{\#6-detector tracks + \#5-detector tracks[i]}} = 1 - \frac{\text{\#5-detector tracks[i]}}{\text{\#6-detector tracks + \#5-detector tracks[i]}},$$

where 5-detector tracks[i] means a track with assigned hits in every detector except the one whose efficiency gets calculated. Time resolution and spatial resolution is measured by the residuals of every hit. The distance between each hit and the predicted point of the track is filled in a histogram for each dimension. If the calibration was done correctly, the distribution is a Gaussian,

[1] 6 detectors with minimum track requirement of 5 detectors

which can than be fitted to get the residual resolutions as the σ of the Gaussian. For real detector resolutions, the fit is redone while ignoring the hit on this particular detector. Including the hit naturally pulls the fit closer to that specific point and hence distorts the resolution. Thus leaving out this hit is a way to determine unbiased resolutions. This result however is also correlated to all other detectors. A bad resolution in one detector leads to a worse fit, which then leads to worse resolutions in all others in the stack. Disentangling this is done by a transformation matrix acting on the vector of correlated detector resolutions.

Chapter 5

Cosmic ray measurements

5.1 Performance tests

The capabilities of an MRPC depends strongly on the gas mixture that is used and the applied high voltage. It is necessary to determine the high voltage work point for a given gas mixture for the detectors in use. This high voltage scan was done by taking data of few hundreds of thousands of events for various field strengths applied in the range of 80 - 120 kV/cm. Another parameter that potentially changes the performance is the threshold of the discriminator. Therefore a scan with varying thresholds from -300 to -600 mV with fixed high voltage was done.
The studied properties were efficiency, time resolution, darkrate, mean cluster size and probability for streamer occurrence. The last one is derived from the ToT distribution that shows a second, high voltage dependent peak that is most likely explained by streamers that occur in the detector. In this context a streamer refers to secondary photons that are emitted by avalanche electrons before ionizing the gas themselves elsewhere, thus creating a second avalanche that gets detected. Streamers typically lead to a much higher ToT, which results in a second peak in the ToT distribution. One can get a rough estimation of the probability of streamer events by comparing the two peaks in the ToT as shown in Figure 5.1. After projecting the ToT distribution onto the y-axis,

the second peak is integrated to get the number of entries, which is then divided by the total number of entries to get a probability. This method is by no means exact and should be treated with caution since the distributions also have tails reaching into each other that are completely neglected. The red lines in both histograms show the same location in 2D and 1D and are located at the minimum, which is considered the border between the 2 peaks. For low field strengths the second peak almost vanishes and therefore the probability quickly reaches zero. The electric field strength in this example is 111,3 kV/cm.

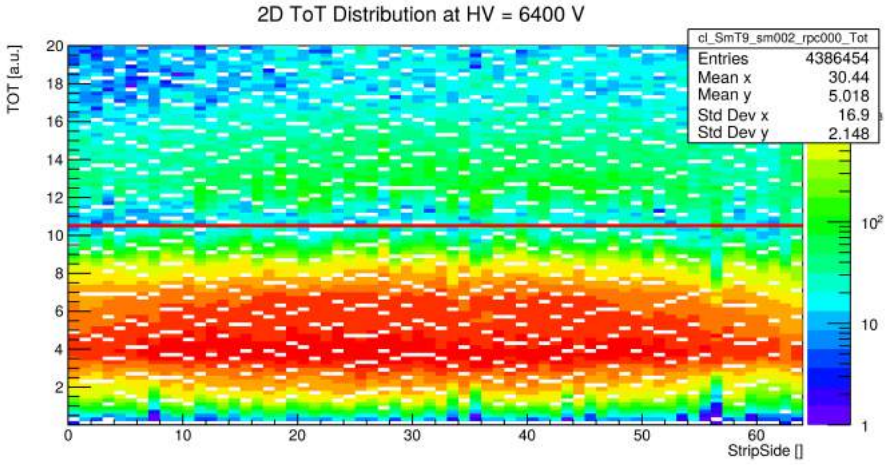

(a)

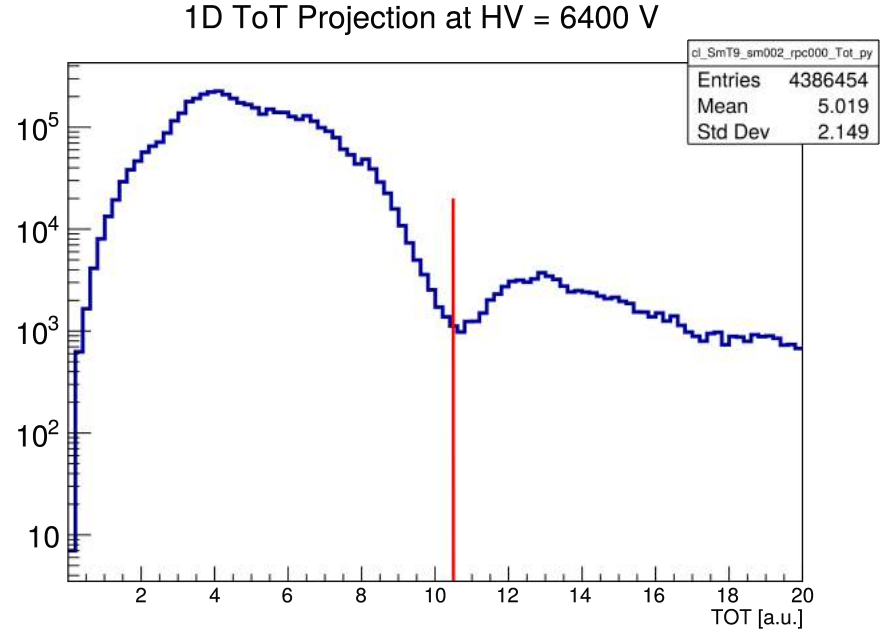

(b)

Figure 5.1: An example of how the streamer probability was estimated. (a) shows the ToT distribution for one detector at a fairly large field strength. The sum of all strip sides results in (b), a projection of (a) on Y. The ratio of both peaks is the estimated streamer probability as a first and simple approximation.

The results of the complete high voltage scan are shown in Figure 5.2a - e.

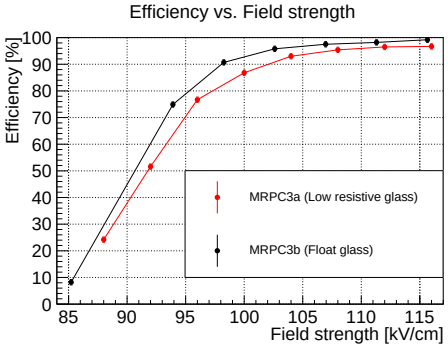

(a) Efficiency

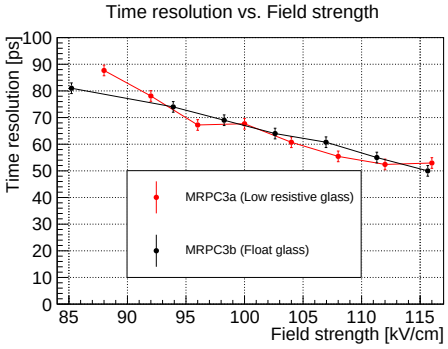

(b) Time resolution

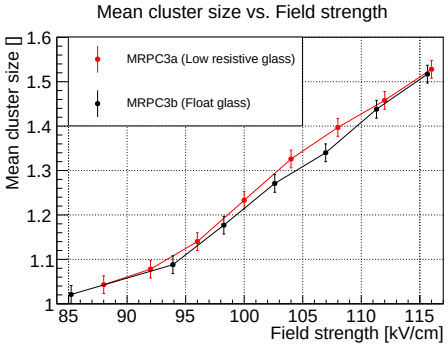

(c) Mean cluster size

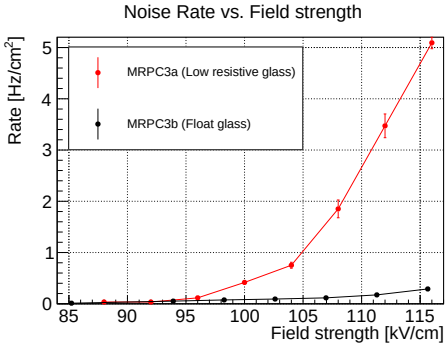

(d) Noise rate/Dark rate

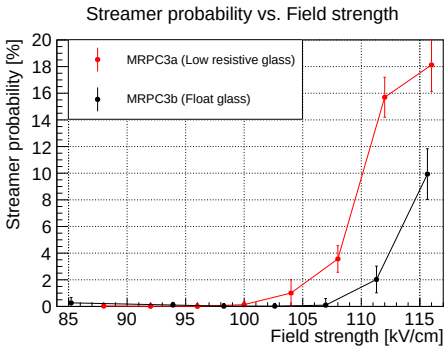

(e) Streamer probability

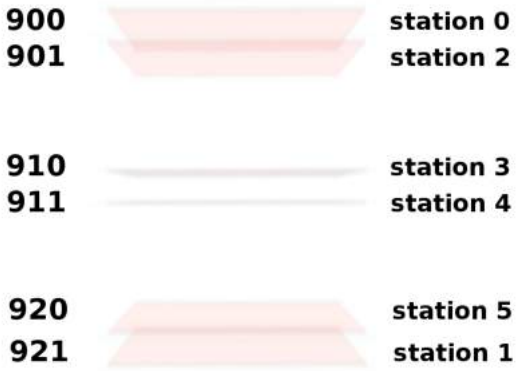

(f) Geometry of experimental setup

Figure 5.2: Electric field dependent detector performances (a) - (e). Efficiency (a), time resolution (b), mean cluster size (c), noise rate(d) and what is assumed as streamer probability (e). (f) shows a schematic layout of how the setup looked with station order in tracking.

The gas mixture used during these testis made up of 90 % 1,1,1,2 - Tetrafluoroethane or R-134a ($C_2H_2F_4$), 5 % Isobutane (C_4H_{10}) and 5 % Sulfur hexafluoride (SF_6). The threshold of the PADI is set to -300 mV for the MRPC3a type from Tsinghua and -165 mV for the MRPC3b type from USTC. For tracking relevant parameters were set to a χ^2 of 3,5 with full angle acceptance and a tracking setup where the first two stations are the outermost detectors. The third one was the detector under test followed by the remaining detectors from top to bottom as shown in Figure 5.2f. First of all one clearly sees a similar behaviour in both MRPC types except for the high rise in the darkrate for strong fields in the MRPC3a. The plateau of the efficiency starts at field strengths higher than ∼105 kV/cm whereas the time resolution still gets better with stronger fields. Furthermore an increase in mean cluster size is expected and with this a higher occupancy of the whole surface is associated. As mentioned before one also observes an expected rise in the darkrate, which is more crucial in the case of MRPC3a as this increases rather rapidly compared to MRPC3b even though the threshold is twice as high. Lastly the measured streamer probability has to be considered that follows the same expected trend and increases with stronger fields. Even though the probability is slightly higher for MRPC3a, both show the same behaviour.

The same procedure was redone while scanning the threshold dependence of the detector performance with fixed high voltage. This was only done for the type 3a since type 3b doesn't show any requirement to increase the threshold as its darkrate is an order of magnitude smaller. The applied voltage for the detector under test was 5,6 kV, which corresponds to a field strength of 112 kV/cm. First of all, if one compares the ToT for different thresholds (Figure 5.3), one sees on the right y-axis that the mean ToT is shorter for higher thresholds as the scale is shrinking. The overall shape, however, stays the same. This verifies that nothing unexpected happens and the setting of the threshold is working as intended.

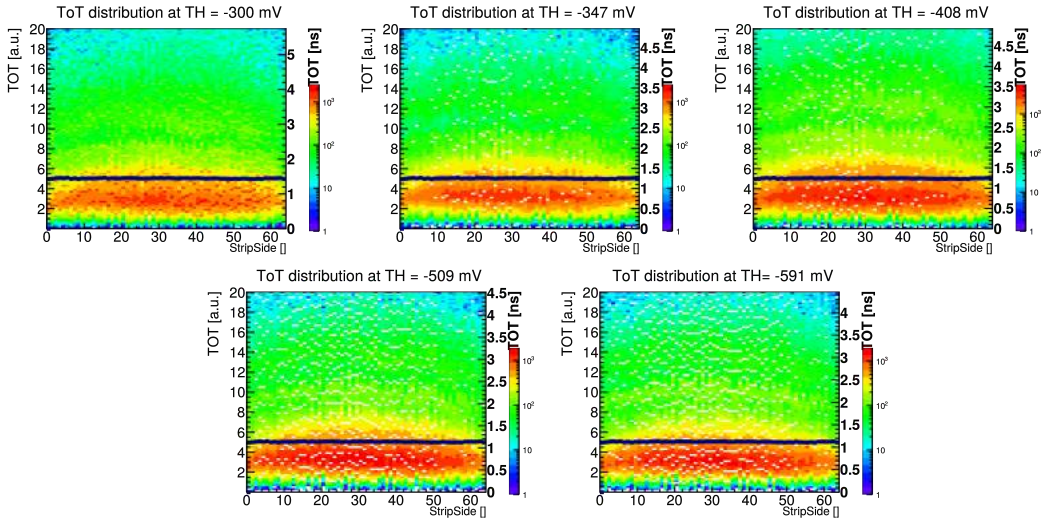

Figure 5.3: ToT of every channel of detector 901. Variation of the discriminator threshold from -300 mV to about -600 mV leads to a reduced ToT as expected but the overall shape stays the same.

The time resolution and efficiency are summarized in a single plot in Figure 5.4. One sees that the efficiency drops for high thresholds by up to 10 % but is more or less flat for a lower threshold. Time resolution wise on the other hand the opposite is the case. The high threshold region is flat while low thresholds have better time resolutions by about 5 ps. The maximum threshold that can be set is 591 mV and going below 300 mV boosts the darkrate over the capability that the DAQ can handle. As conclusion, this scan's results show the possibility to increase the threshold up to 400 mV when needed. This can be used to suppress high noise rates without losing too much performance. Anything further, however, is not recommended as the detector gets inefficient to a point where reasonable operation is not possible anymore.

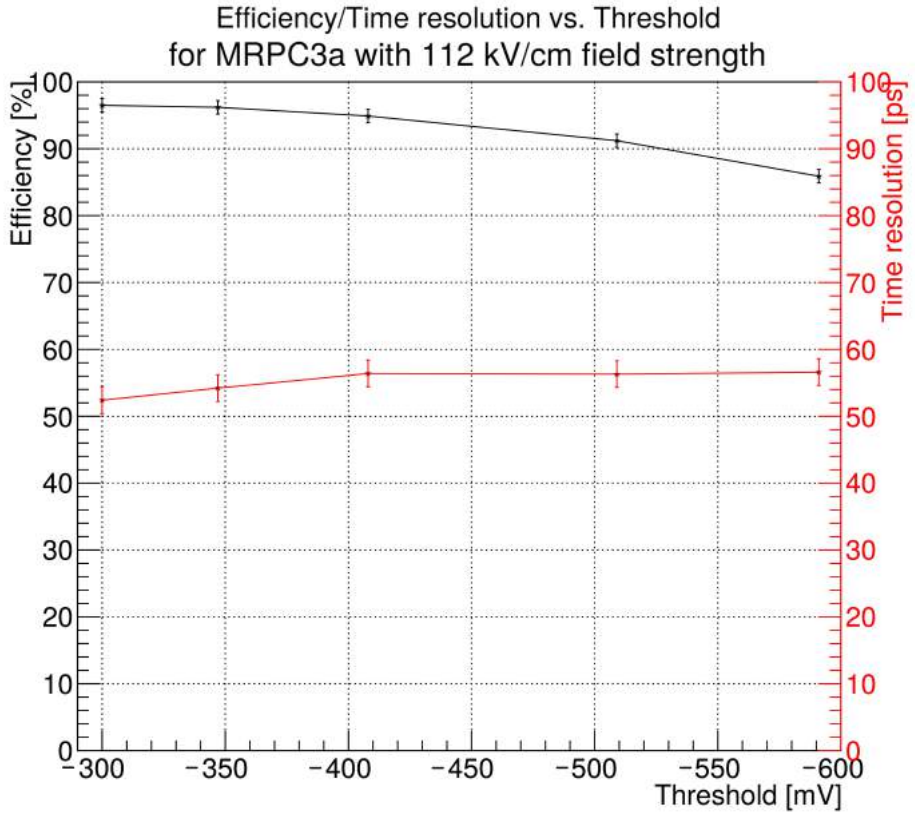

Figure 5.4: Efficiency and time resolution dependence on the threshold. Efficiency is more affected by higher thresholds than time resolution. Potential increase to -400 mV would be acceptable if noise needs to be suppressed.

However, while analysing the data it became apparent that the tracker itself is not entirely optimized for working with cosmic muon events. As mentioned before, the tracking setup and therefore the order of the detectors play a role in the results. This is clearly a software artifact that should in the ideal case not affect any derived quantities, since this order has no physical implications and is just a way how the software handles the calculation. To investigate this further, the same run was repeatedly analysed with just a changed tracking setup to help understand what could cause this. The field in both MRPC types was 111 - 112 kV/cm with a threshold of -300 mV for type 3a (900, 901) and -165 mV for type 3b (910, 911, 920, 921). Sometimes the detectors have

multiple data points in the same location. As a result of various permutations in the tracking setup, analysing the same run generates partially two or three measured points for a detector at the same station. Results can be seen in Figure 5.5.

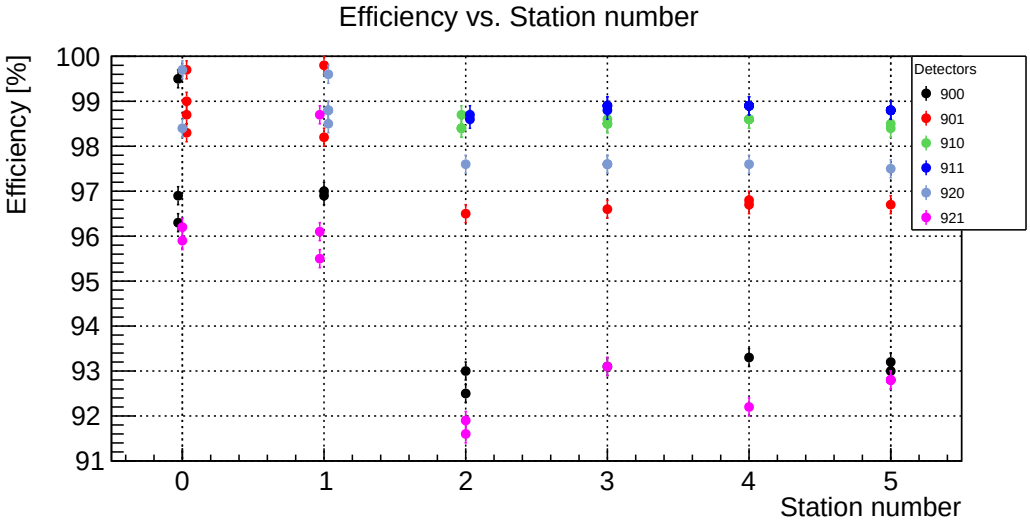

(a)

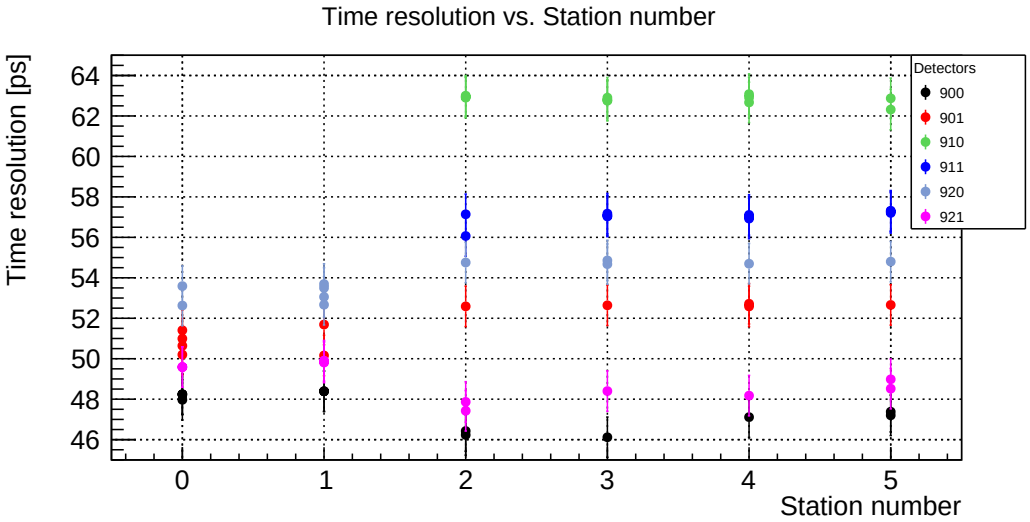

(b)

Figure 5.5: Efficiency and time resolution as a function of the tracking setup station. If a detector is on position 2 - 5, the results are consistent within the uncertainty. If it is on position 0 & 1 that define the tracklet-seed, the results differ significantly from the other stations' and even among themselves if measured multiple times.

The data shows a clear difference between station 0 & 1 and the rest that follows. Especially for efficiency, the first two stations fluctuate heavily whereas station number 2 - 5 are very consistent for every detector and show independence. Same holds true in the case of time resolutions. Although less for stations 0 and 1, the resolutions differ from the ones where the detector sits on station 2 - 5. Again, a flat and independent trend can be observed here, too. What is furthermore interesting in these plots is the fact that not only the first two station vary from the rest, but also that the different detectors have completely different characteristics. In theory, the first two (900, 901) and the last 4 (910, 911, 920, 921) are built equally and should therefore perform in exactly the same way. For better visualization, Figure 5.6a shows the efficiency of every detector, obtained by averaging over the above results for the stable stations 2 - 5. Figure 5.6b shows the same but for time resolutions.

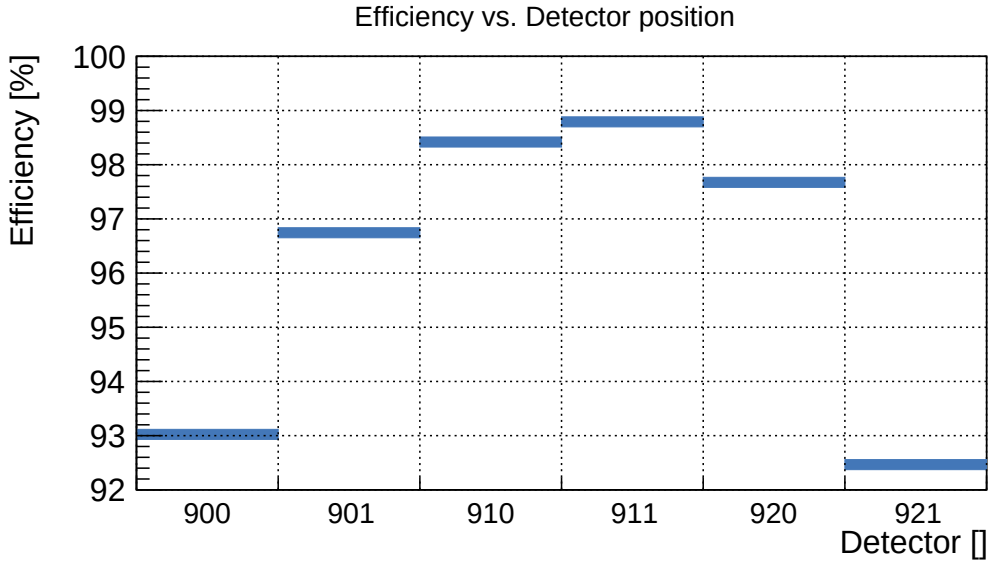

(a)

(b)

Figure 5.6: Efficiency and time resolution as a function of the detector and thus the physical location in the stack. Inner detectors perform better in terms of efficiency but are much worse when it comes to proper timing. The outer ones behave exactly opposite, with good time resolutions but reduced efficiency.

What can be deduced from this is a massive increase in efficiency for detectors that are physically in the middle of the setup with respect to the outer ones, whereas the time resolution is getting worse by more than 10 ps. This either shows that small differences in the production of the detector have an underestimated impact on their later performance or that there are inconsistencies in the software causing this. Similar observations can also be seen in simulations where one can just set the detectors to be exactly equal in all aspects [3]. This then implies that the tracking algorithm treats the detectors differently depending on their physical location.
Simultaneous decrease in efficiency and increase in time resolution can also be seen with more narrow cuts in the χ^2 and broader cuts have the opposite effect. So for outer detectors, the same globally defined χ^2 seems to select more strictly than it does for the detectors in the middle of the stack. This can be understood if one assumes the same errors for all detectors. Also assume a reconstructed track that slightly differs from the original particles path of flight. Moving away from the midpoint then means larger distances between the data points and the reconstructed track as the lever arm gets longer. With a given standard deviation, the outer points are relative to this deviation further away and more likely to fail the acceptance limits.

5.2 Angular Analysis

In the end it is also interesting to look closer at the angular behaviour and how the observables depend on the angle of the track. The coordinate system is defined such that the azimuthal angle ϕ describes rotations in the x-y-plane ranging from 0 to 2π. The polar angle θ is defined as the angle away from the z-axis ranging from 0 to $\pi/2$ since only forward direction is relevant. For better visualization, Figure 5.7 explains the coordinate system pictorially. $\phi = 0, \pi, 2\pi$ means a movement in x-direction (across the strips) and $\phi = \pi/2, 3\pi/2$ is directed towards the y-direction (along the strips). On the other hand, $\theta = 0$ represents a vertical track, perpendicular to the detector plane and the

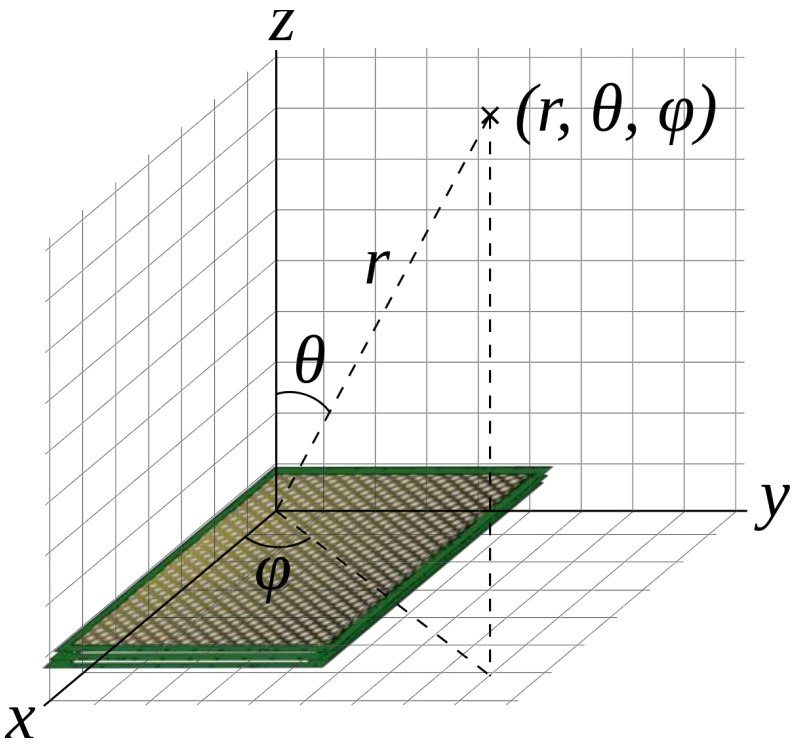

Figure 5.7

ground surface. Higher θ angles correspond to higher inclinations. Against both of these angles, a various set of observables was plotted in histograms and analysed. At the very top of all figures, the respective observables distribution under all angles is presented. The second histogram then shows the projection of the above histogram on y-axis to see the total distribution of the measured quantity. Yet, in case of cluster size it makes more sense to project on the x-axis to see the total angular distribution of all tracks. The third and forth plot reveal the mean and RMS of all the angle bins in the first 2D histogram, respectively. For time and space coordinates, a gaussian curve was fitted to every bin, which gives a standard deviation to replace the RMS if the fit converged. The statistics is based on all tracks with hits in every station. This makes up 160.000 tracks with 6 hits each, so a combined statistics of 960.000 measured points were used.

5.2.1 Cluster Size

From the distribution a maximal acceptance angle of about 43 ° is immediately visible. This fits the geometrical constraints of an active volume of 27 cm width, 32 cm length and 44 cm height. Another interesting observation is the minimum at 0 ° in the second plot even though cosmic rays come preferentially down vertically. This comes from the vanishing phase space for particles coming straight down which then increases for larger angles. Combining this geometry dependent phase space factor with the known $\cos^2(\theta)$ behaviour leads to the measured distribution. What shows up in the last two plots can also be understood quite well. In theory, a particle that crosses the active volume of an MRPC covers a larger distance inside with greater inclination. In such cases it is more likely to induce a signal on more strips simultaneously which culminates in larger clusters on average. The mean cluster size proves this true as it gets significantly larger for larger θ. The RMS stays constant at all angles and indicates a constant cluster size spread among all angles.

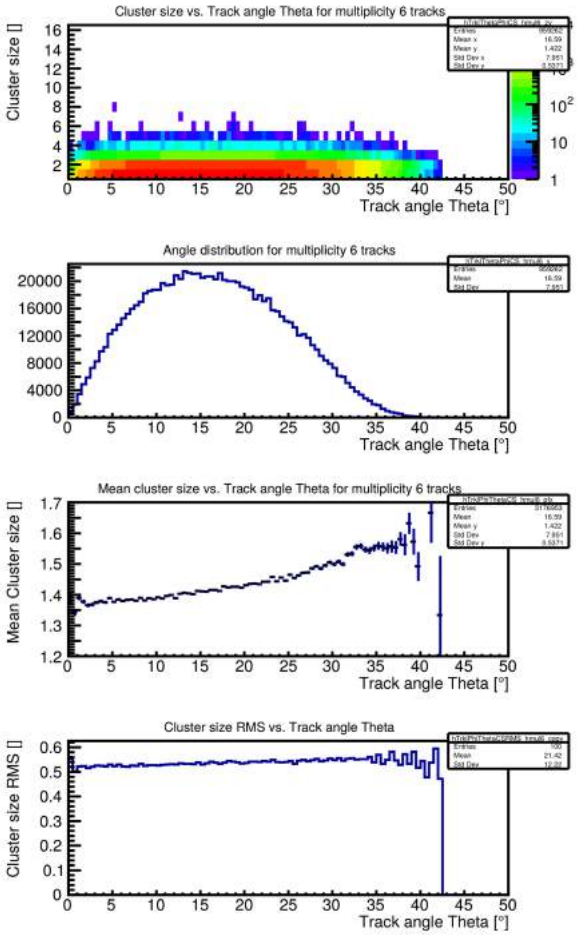

Figure 5.8: Cluster size dependence on theta angle for 6 hit tracks.

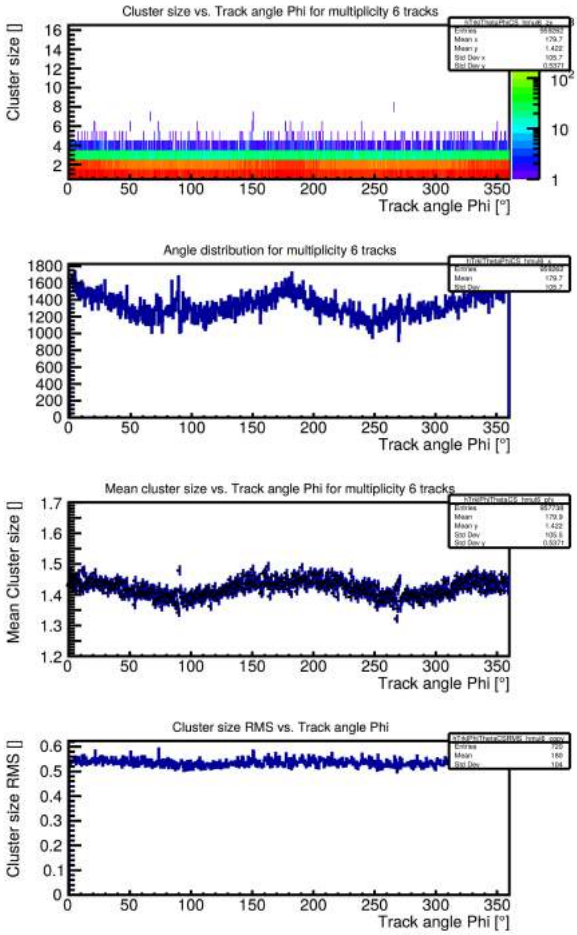

Figure 5.9: Cluster size dependence on phi angle for 6 hit tracks.

Similar to the θ dependence, ϕ also affects the cluster size. The first assumption would be equally distributed angles since cosmic rays are ϕ independent. Taking into account the different lengths in x (32 cm) and y (27 cm), this again gives a phase space factor that raises the probability for finding tracks in the longer direction, $\pm$ x, represented by $\phi = 0\,°$, $180\,°$, $360\,°$. Along these angles, the mean cluster sizes also exceed the values at $90\,°$ and $270\,°$ in-between. This can be understood by also including varying polar angles. A track along y will cover no distance in x regardless of its polar angle. For trajectories along x, this is not the case. There, a larger polar angle will lead to the same rise in mean cluster size as indicated before (Figure 5.8). Again as before, the RMS shows no dependence on ϕ at all.

5.2.2 Time over Threshold

The second observable was chosen to be the time over threshold. The ToT is a measure of the avalanche's build up charge. Besides many other factors it gives a rough estimation of the primary particles' energy depositions. What can be seen on Figure 5.10 is the accumulated ToT, which is the summed up ToT of all participating strips in the cluster. It is therefore not surprising that the same dependency as before for the cluster size can be observed, as it is directly related. In the second histogram one notices a pronounced peak at a ToT of 6. This is the contribution of the cluster with cluster size 1. The smaller side peak at roughly 9 belongs to cluster size 2. Everything above that can not be resolved in this plot anymore, because of lacking statistics.

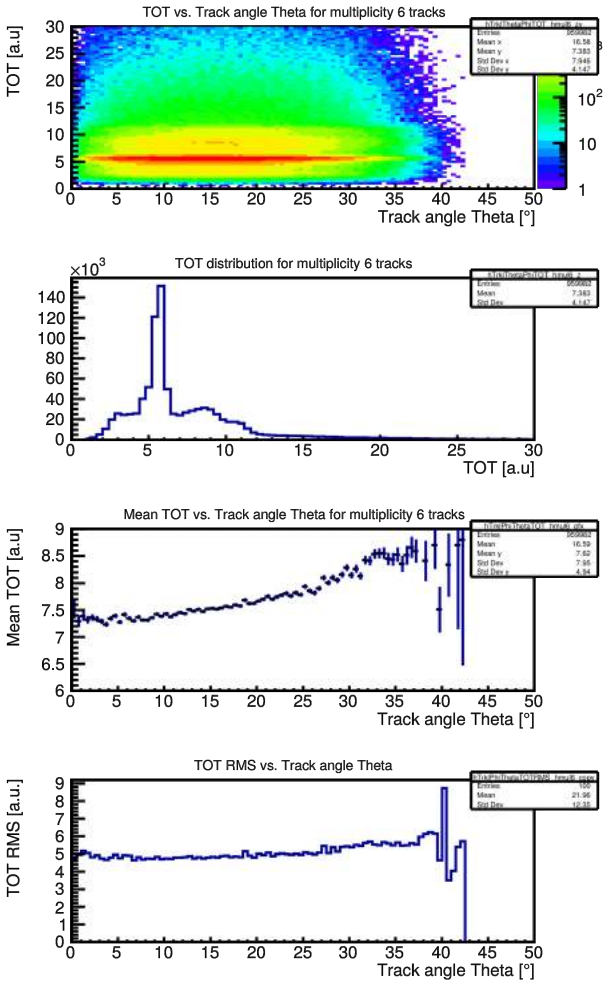

Figure 5.10: Time over threshold dependence on theta angle for 6 hit tracks.

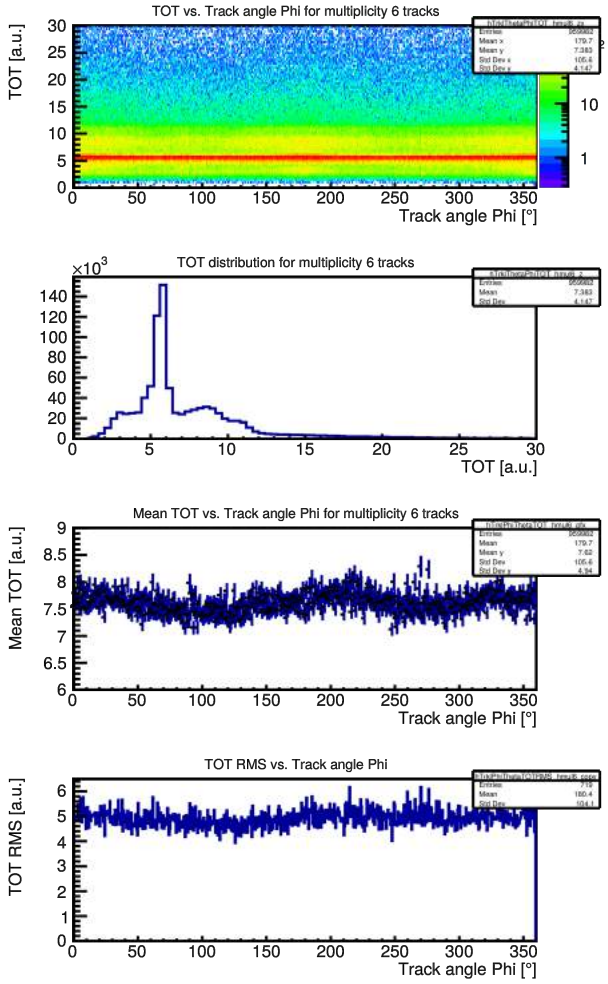

Figure 5.11: Time over threshold dependence on phi angle for 6 hit tracks.

Looking at the ϕ distribution confirms the assumed connection to the cluster size. The same behaviour of the mean is present with its slight enhancements along x-direction, too. This enhancement is caused by the secondary peak, coloured yellow in the top histogram. The red main peak stays the same while the first side peak is more pronounced in $\pm$ x. Every bins' RMS is constant and proves again no connection to ϕ. It is worth noting that the main peak in the ToT distribution is not located at a value of 5 a.u but rather at a value of 6 a.u. The calibration should shift this to a value of 5. The data used for calibration still includes all the detector noise, which is typically low in ToT that reduces the mean ToT. Signals from real particle alone tracks seem to be much higher and thus longer in time.

5.2.3 Average Time over Threshold

To see whether the ToT in itself shows any dependence on the angles it is necessary to look at the average ToT. It is the same measured quantity as above but additionally divided by the cluster size of the hit. The most notable difference is that the mean averaged ToT's trend disappears and it is roughly the same for all observable polar angles. It seems likely that a connection to cluster size is the main contribution to a non-flat angular behaviour. The second big difference to the accumulated ToT is visible in the second plot. Besides the main peak, the overall ToT distribution shape changes fully. Its position is at the same two bins with roughly the same height.

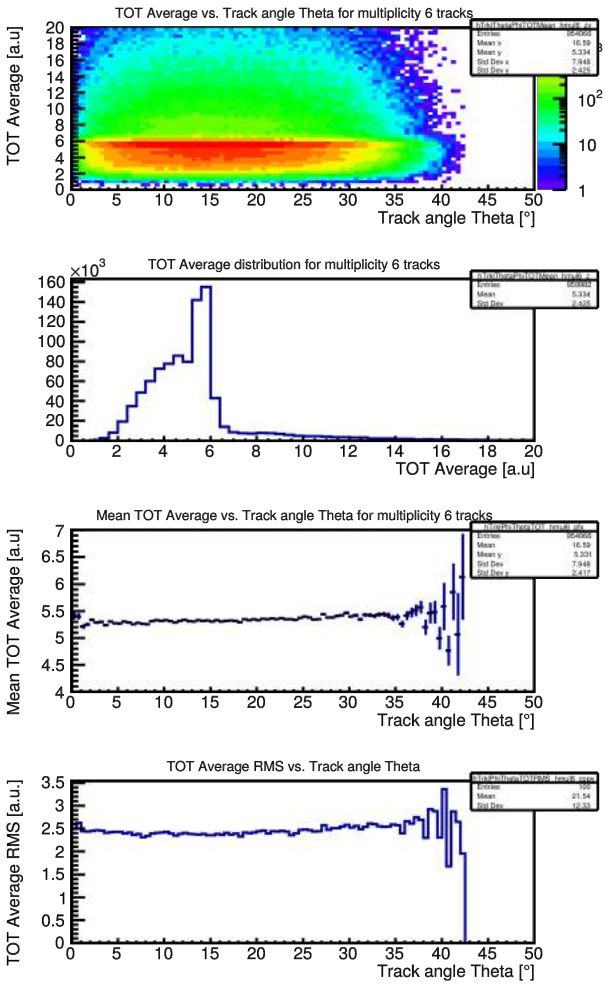

Figure 5.12: Average time over threshold dependence on theta angle for 6 hit tracks.

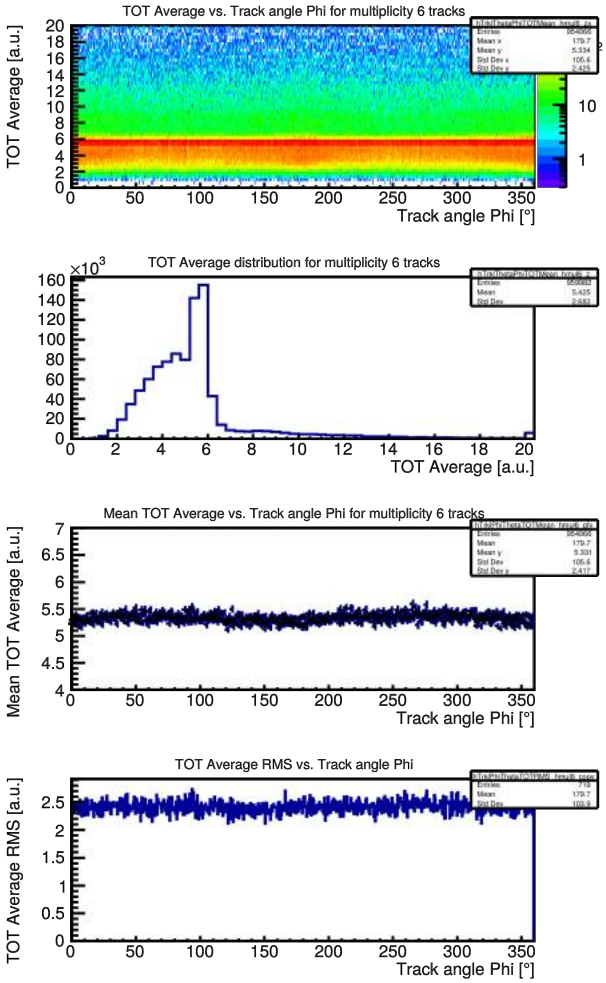

Figure 5.13: Average time over threshold dependence on phi angle for 6 hit tracks.

This confirms that they indeed belong to hits with cluster size one. What's left is the remnants of larger cluster size hits. Typically, only the center strip of a cluster has a high ToT, following the usual distribution. Neighbouring strips see a smaller and therefore shorter pulse. After averaging this sum of ToTs over the cluster size, the larger the cluster is the smaller the average ToT becomes. Taking the second peak of the accumulated ToT at about 9 a.u. and dividing it by the assumed cluster size of 2 this gives 4,5. And indeed, in the average ToT distribution one finds such a small enhancement between 4 and 5. The results from the ToT measurement are therefore well understood.

5.2.4 Time resolutions

The quantity of most interest for building a Time-of-Flight wall is the time resolution of the system. By ignoring the hit of the respective detector for the track fit, an unbiased resolution is achieved in contrast to a biased residual. It immediately becomes apparent that the global mean-shift to zero also holds true for all angles individually to a very high precision. The systems overall time resolution is in the order of 50 ps, which is an excellent result. A little unexpected though is the improvement in resolution of 10 ps from 55 ps down to 45 ps for stronger inclined tracks.

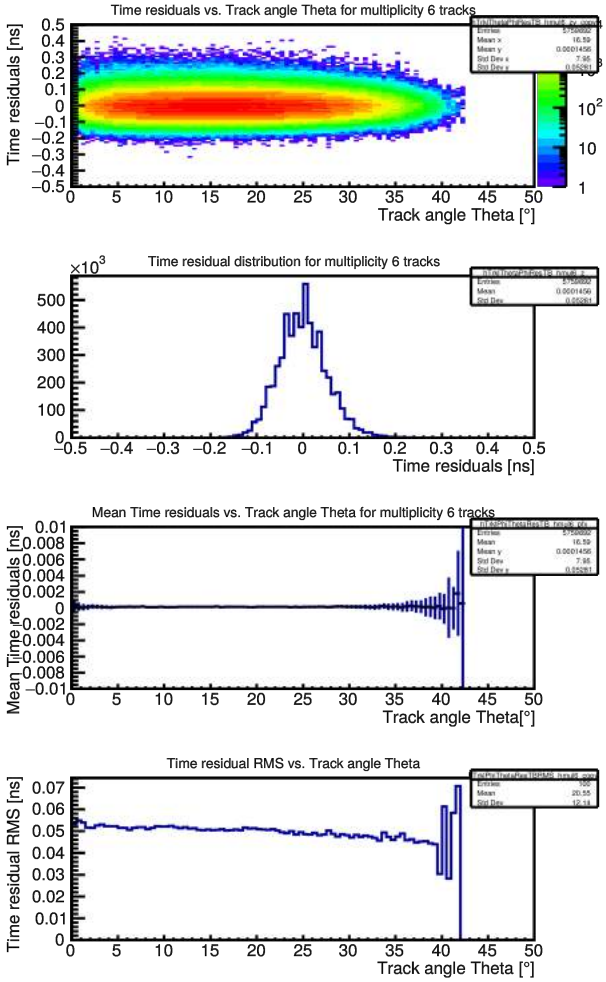

Figure 5.14: Time resolution dependence on theta angle for 6 hit tracks.

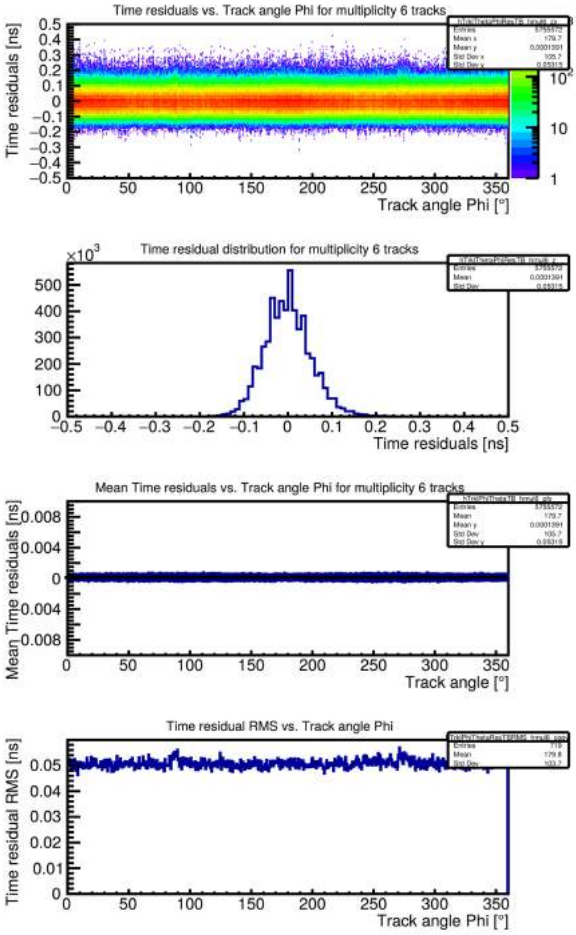

Figure 5.15: Time resolution dependence on phi angle for 6 hit tracks.

Based on what can be seen in the ϕ plots this is not related to cluster size. Otherwise it would also show a lower resolution in the $\pm$ x-direction. The ϕ angles show no dependence at all which is immensely advantageous. Averaging over θ gives a system resolution of precisely 53 ps. Again no mean shifts are observable and as stated before, the resolution is the same for all azimuthal angles. All in all, time resolution wise everything looks promising and except minor variations for θ it is as stable as desired.

5.2.5 X Residuals

For track matching the spatial precision is of interest. Starting with the x-coordinate, the residuals are plotted against θ and ϕ. As for the time resolution, the globally applied mean-shift holds true for all angles in x-direction individually, too. It can be seen by the flat zero line in the third histogram. The global residual width is 2 mm. This is in the order of $1\,\text{cm} \times 1/\sqrt{12}$ that one expects for a strip with 1 cm pitch. For higher inclinations, the widths become worse by roughly a factor of two. Nevertheless, the overall precision is still within expectations. It is, however, worthwhile to think about what could causes this rise in width. A track coming at $\theta = 0$ leaves a point when projected on the x-y-plane. For $\theta \neq 0$ this is a line, due to the detectors extension in z. Consequently, the hits point-like treatment in the software does not represent the physical path projection and adds to the uncertainty.

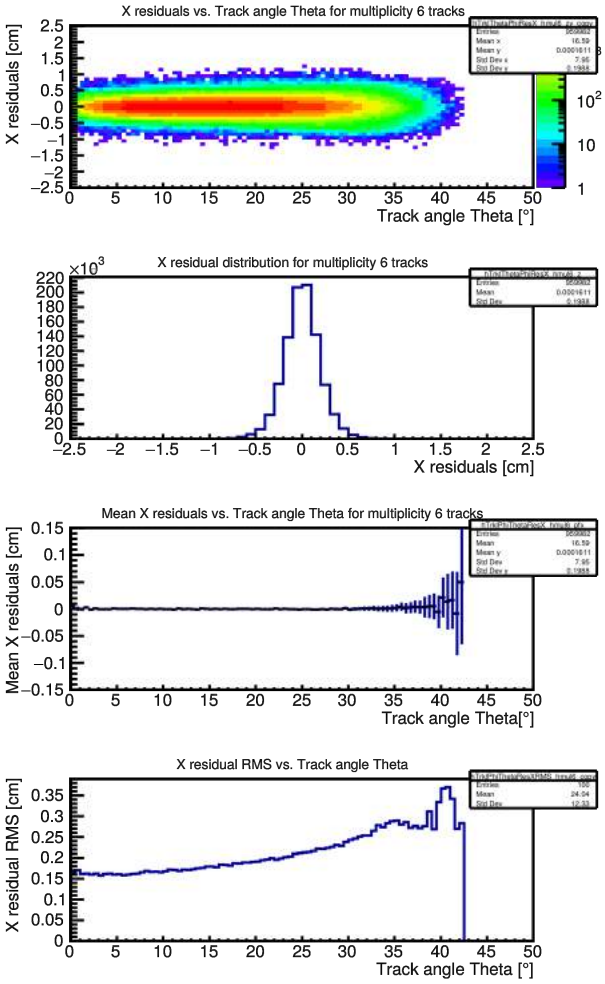

Figure 5.16: X residual dependence on theta angle for 6 hit tracks.

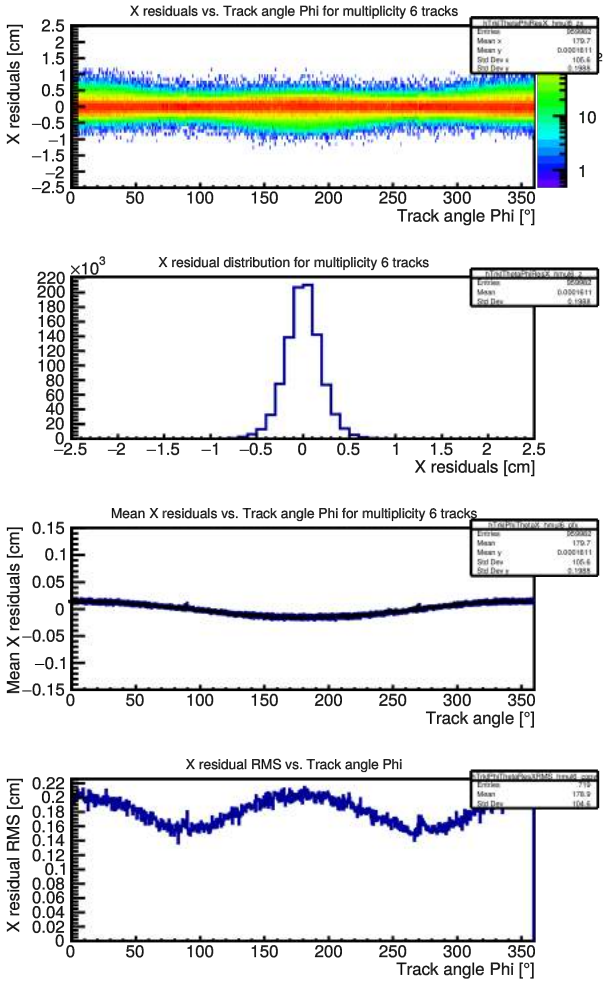

Figure 5.17: X residual dependence on phi angle for 6 hit tracks.

A look at what happens under variation of ϕ supports this hypothesis. In x-direction, the x widths are worse than in y-direction. The Δx for a line, directed towards y is the same as a point's.

The mean distribution for ϕ is not flat but has deviations from zero along x. In the first plot one sees that the mean (red band) is always centered around zero but the tails extend more to one side along x. This effect is in the order of $1/10$ mm and very much negligible. However, it has to be emphasized how accurate one can measure such tiny deviations and investigate even smallest trends in performance.

5.2.6 Y Residuals

Continuing with the y-coordinate, the following plots show the y residual behaviour under varying angles. Here, everything is almost exactly the same compared with the x residuals. The widths of the y residual distributions are mostly predominated by the signal's propagation time and therefore the time measurement. A possible increase in width due to point-like treatment is hardly visible and could also be a statistical effect. The global residual width for the y-coordinate is 3 mm. This coincides with the statement from before which was calculated by using the electronics' time resolution and the signal's propagation velocity. Going further to the ϕ distributions, the differences become apparent here, too.

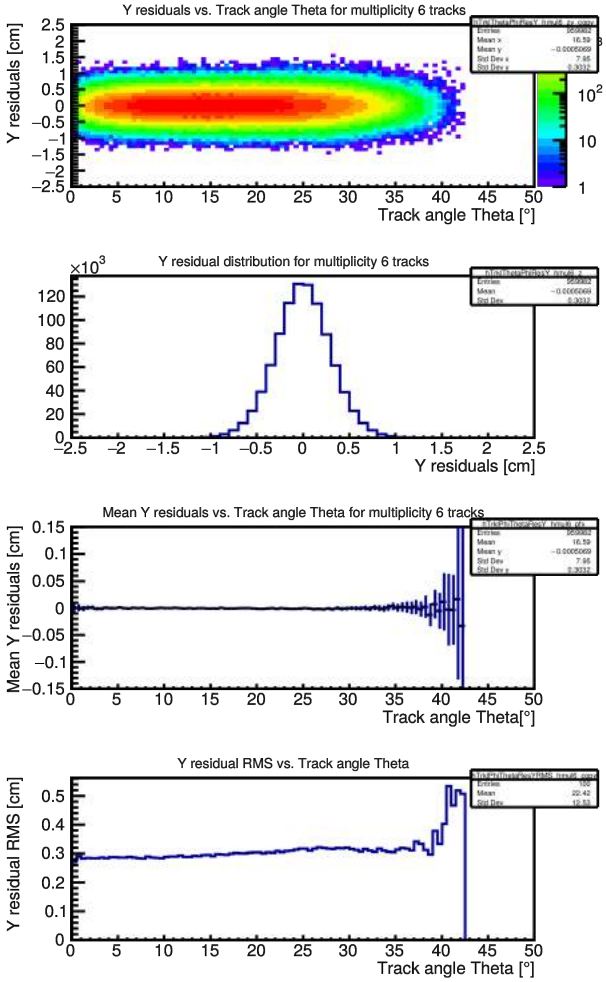

Figure 5.18: Y residual dependence on theta angle for 6 hit tracks.

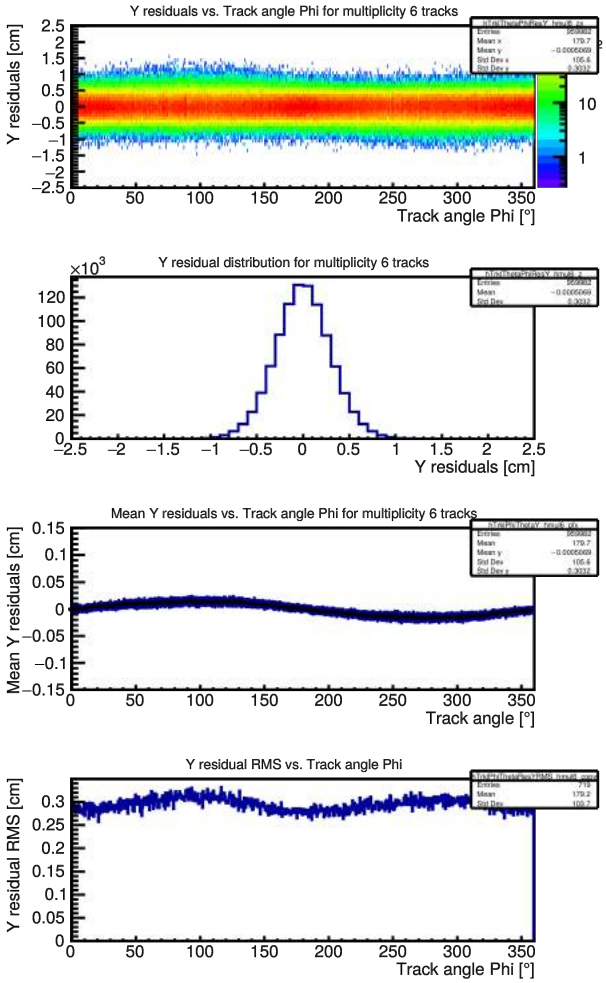

Figure 5.19: Y residual dependence on phi angle for 6 hit tracks.

As before, but with a $\pi/2$ phase shift, the mean deviates from zero not along x, but along y. For $\phi = \pi/2, 3\pi/2$ the widths are also a little bit larger. Applying the hypothesis about the smearing for higher inclined tracks on this, the results match the expectations quite well. Interesting to note is that for both, x and y, the one sided tails that lead to the mean shifts are on the positive side for +x/y-direction and vice versa. This could imply that the avalanche in the lower part of the MRPC has a higher impact on the signal, because it is shifted more towards the direction of flight.

To summarize the observed results, a better than expected system time resolution of ∼50 ps was achieved. Spatial distributions are determined very precisely, too. With widths in the order of mm this fits the requirements that are needed. The ability to see such small fluctuations proves again that tracking provides a strong tool in examining detectors. These results give a first glimpse of what to expect in the final CBM experiment, which will cover angles from 2,5 ° - 25 °. This also means that relatively strong effects like e.g. cluster size growth will be less pronounced than it is shown before.

5.3 Differential Analysis

In this section, another way on how to probe what is happening in an running MRPC is presented. This is done by the before mentioned differential analysis in which the detector itself is divided in smaller cells to see not global but local parameters. This method is however limited by the amount of statistics in each cell. With the low rate of cosmic events, compared to accelerator test beams one accumulates only a few hundreds of thousands to few million events with the used solid angle in reasonable time. Dividing the whole detector surface of $32 \times 27\,\mathrm{cm}^2$ in $1\,\mathrm{cm}^2$ large cells leads to roughly 3 orders of magnitude less statistics per cell. This ends up with only a few thousand events and therefore significantly higher statistical error. Figure 5.20a - c depict these results for the time resolution (a), position resolution in x-direction (b) and y-direction (c). The example chosen here is station 2. This is the same station of the detector under test in the previous sections. In this case it is 901 (Figure 5.2f) that is presented. The whole set of histograms also for the other detectors can be found in appendix A. The detectors are encoded from top to bottom in their station numbers 0 - 5 as before (Figure 5.2f). The number of tracks going through a certain cell is shown in the left column. In the middle column one sees the mean of the gaussian that is fitted onto the residuals of every hit. Mean shifts can be hints for some systematics that are not yet considered in the analysis or building process. On the right side is the variance of this fit

that shows the resolution, which should be the purely statistical uncertainty if the calibration was done correctly. It should also be mentioned that the electronics in the last station (920) did not work properly for two strips, which are therefore populated less.

These histograms (Appendix Fig A.1) contain a lot of information about the detectors. First of all one should disregard the outermost cells since the left side plots show that they clearly lack statistics to ensure trustworthy results. What's interesting resides in the center cells where most of the statistics lies. Even though most of them were build equal, they perform in some regards totally different. Timing wise it looks mostly of what one expects, namely means that gather around zero with little deviations, making the histogram look homogeneous. The variances range from 50 - 70 ps, if one neglects the edges, and confirm previous observations about worse resolutions for inner detectors. Despite the colour making it look more inhomogeneous, the deviations within a detector are fairly small.

The x-coordinate related histograms however show unexpected behaviour that are not fully understood yet. At first glance the mean shifts also look homogeneous for most of the stations, but all share the feature of a gradient along the x-axis with both, a positive and negative slope. Especially strongly pronounced is this in the second (921) and last station (920) that are physically on the bottom of the stack. The last station also shares a much worse x-resolution that is twice as high as that of the rest.

The y-coordinate histograms show the same kind of behaviour. Again it can be observed that the mean shifts follow some trend that is now not along the x-axis but rather the y-axis. In this regard no station stands out, but for the resolution, station 5 shows again a way worse result than the others. Even after switching the electronics and redoing the tracking with a different setup, this behaviour persisted. Since there is no reason to assume that this should be a feature of the second last detector in the stack, it would be safe to assume that the detector itself has some fundamental problem in its spatial resolution capabilities. Though, the cause of this was found several months later. When opening the module to exchange the detectors, a construction error became

apparent. The fixing bars of the detector were flipped upside down which resulted in roughly 2 cm deviation in z-direction compared to the assumed geometry. Considering an average theta angle of 15 ° gives a x & y displacement of up to roughly 5 mm. This broadens the residual distribution and leads to larger widths.

Another interesting feature, especially in the y-coordinate plots, is the presence of strip structures. One can now speculate whether this comes from significant deviations in single channel performances on the same PADI chip or bad electrical contact on the detector itself, e.g. poor soldering of the strip.

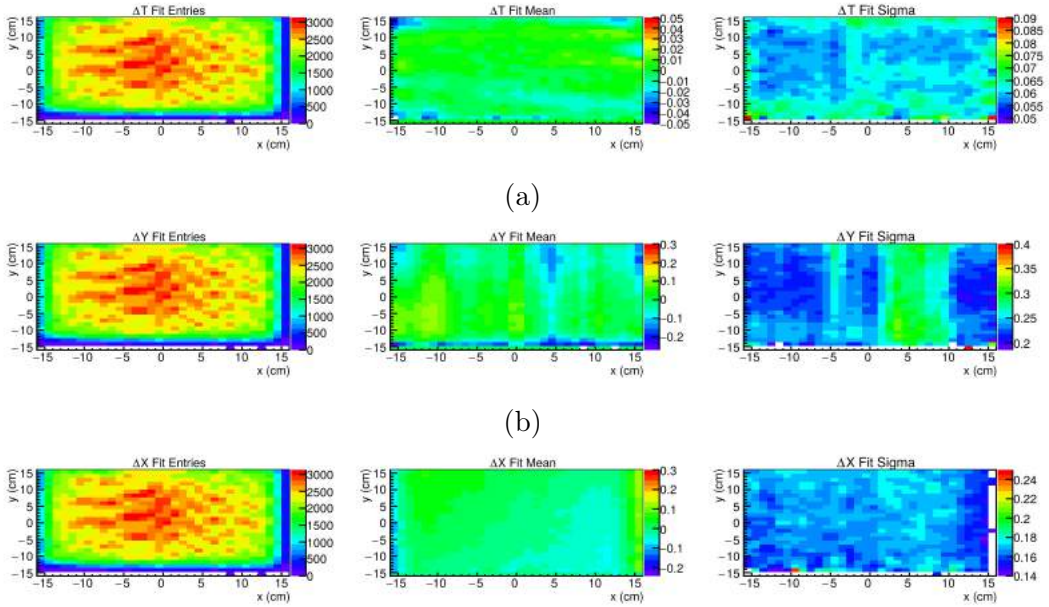

Figure 5.20: Differential detector performance. Left column shows the hit distribution in the detector. The middle column is the mean shift from zero of the residual distribution and the right column contains the respective residual width. Depicted is this for time (a), x position (b) and y position (c).

To emphasize these gradients that visually vanish to some degree in the colour coding, the next plots (Figure 5.21) show the profile of the respective mean shifts of all the detectors on the x-axis (Figure 5.21a) and y-axis (Figure 5.21b).

It shows clearly what was described before. In addition, without exception, every curve crosses the zero mean shift at the center of the detector and every curve is antisymmetric. The effects on the edge can however be neglected due to unreliably low statistics for most of the detectors. A positive slope in the center means that hits are being pushed away from the center while a negative slope means that hits are being pulled towards the center. This applies for both coordinates, x and y, likewise. Shifts in the y-coordinate could be explained by deviations in the signal velocity, since the observed shifts are within the uncertainty of the velocity calibration. However, the x-coordinate is not affected by this and cannot be explained by velocity uncertainties. Simulations showed similar results in the y-coordinate but not in the x-coordinate, however in y an order of magnitude larger. This could be taken care of by fixing the default velocities. Afterwards the mean shifts were perfectly flat also for y. Due to absence of this observations in ideal case simulations it is most likely not a software induced characteristic but rather detector related or stemming from other environmental influences. The most pronounced structure comes from detector 920. Since this detector was placed 2 cm above the geometrically assumed position, the observed mean shifts as well as the slope match this explanation quite well. Thus, an explanation for both coordinates would be an error in the positions used to create the geometry file. Indeed, there, a simplification was made that causes a 1 - 2 mm misalignment along the z-axis, which would be way below the resolution in this direction. This would explain perfectly a gradient of a few millimeter for angled tracks away from the center. So the y mean shifts can be explained by velocity corrections but the combination of both coordinates suggest a geometry induced effect. It is astonishing how sensitive the measurement is to displacements in z, but nevertheless, the arising shifts are all in the sub-millimeter regime that can be neglected for the given system resolution.
This shows that one needs to create the geometries as precise as possible and construct it accordingly.

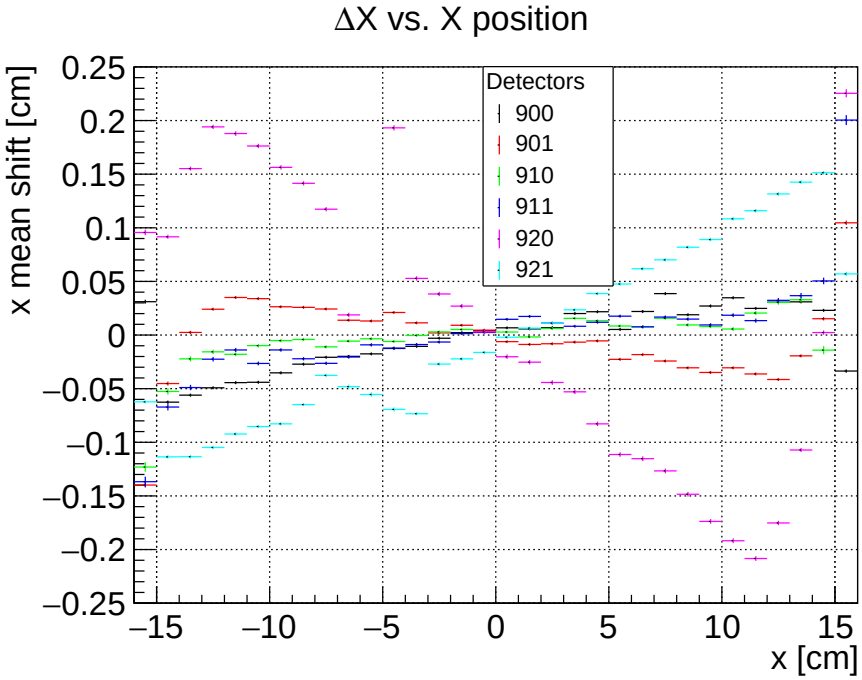

(a) Mean shifts from zero of the x residuals across strips (x-direction)

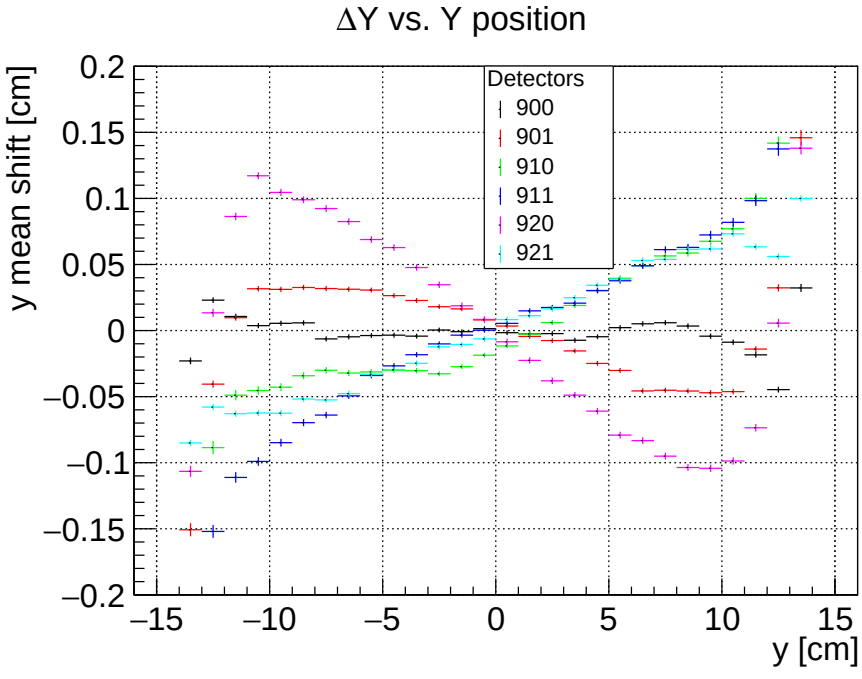

(b) Mean shifts from zero of the y residuals along strips (y-direction)

Figure 5.21: Gradient structure of the mean shifts for x (a) and y (b). Mainly detector 920 stands out with a non flat behaviour, but all are to some extend not flat. The curves are totally asymmetric and cross at zero, in the middle of the detector.

5.4 Event Display

Next to the aforementioned methods there is also the event display. It shows what is happening in the 50 ns of a single event in a graphical interface. This can be used to check what the tracking algorithm is doing and where improvements are necessary. Furthermore it is helpful to get a feeling of the dimensions at which the analysis is working by seeing the models. The already included features can partly be seen in Figure 5.22a. The arrival time of every hit is encoded in its shades of colour ranging continuously from 0 ns (violet) to 50 ns (red). The size of the spheres representing the hits encode that hit's cluster size. The colour of the track line gives information whether 6 (light blue), 5 (violet), 4 (dark blue), or 3 (green) hits are included in this track [4]. Figure 5.22a is also a rare case of an event with a lot of hits and reconstructed tracks. Most of the events contain a single track at most and only a few exceptions show large track multiplicities. The most probable source of this would be interactions somewhere above the stack and a detection of the resulting shower. Though this requires the extended track lines that point upwards, to converge at some common vertex. This could not be observed yet, but is without doubt fascinating to study. Upon closer inspection it is also clear that the tracker reaches its limit in reconstructing multiple tracks per event. It is not designed for omnidirectional cosmics, but rather for beamtime measurements with a common vertex. The additional degrees of freedom, arising from all possible origins, lead sometimes to reconstructions that are not reasonable anymore. A check by the human eye reveals the mismatching tracks that occur with too many hits close in space and time.

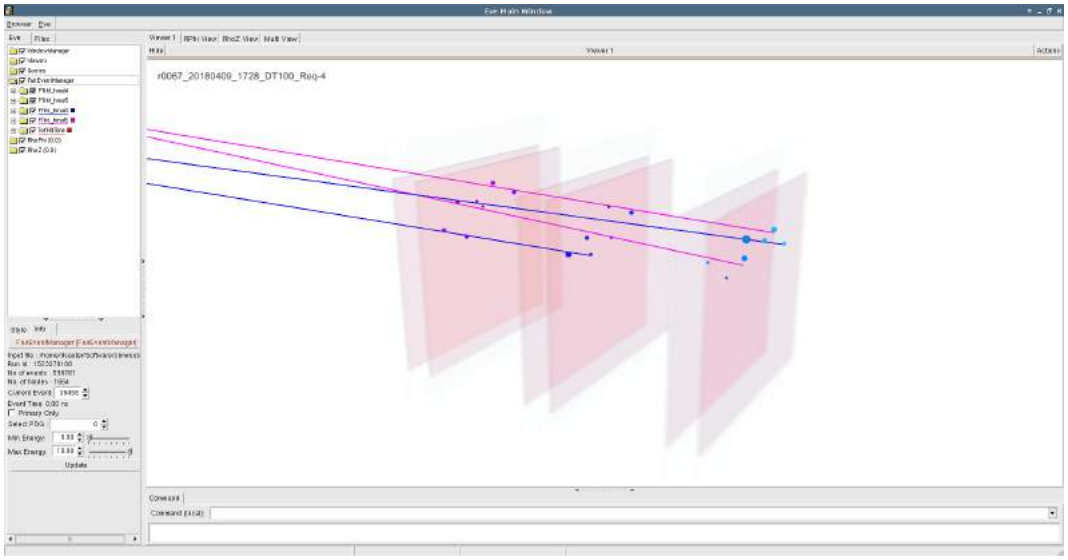

(a)

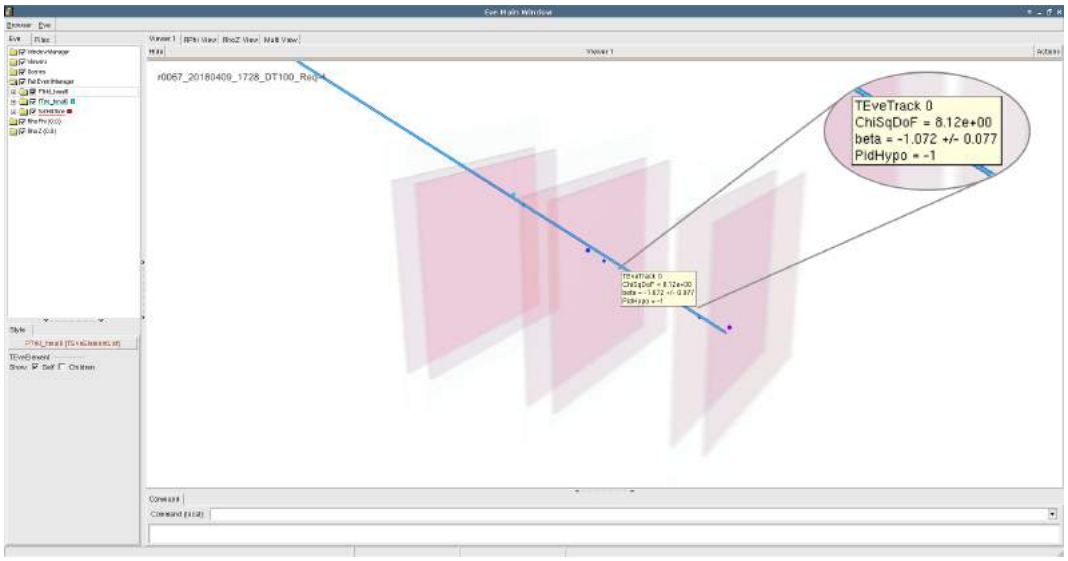

(b)

Figure 5.22: Example pictures of the event display GUI. (a) shows the kind of event with many particles coming at the same time. In (b) one sees at first glance a normal straight track. Further inspection reveals a negative velocity, which means the particle came from below the detector flying upwards.

5.5 Particles from below

The second Figure, 5.22b, shows an even rarer type of event. Positioning the cursor on top of the track line shows a window with additional information about the track, especially the calculated particles velocity in units of the speed of light. In only a few permille of the events one gets a negative velocity meaning the particle traversed the detectors from below. From naturally occurring radiation, only cosmic muons are able to travel through the entire stack and deposit energy without getting stopped in or somewhere before the system. It is however impossible for a muon to travel through the earth without getting captured at some point.
One possible explanation is therefore a muon neutrino ν_μ that traverses the earth and interacts with either electrons or neutrons in the last few hundred meters of rock under the institute in such a way:

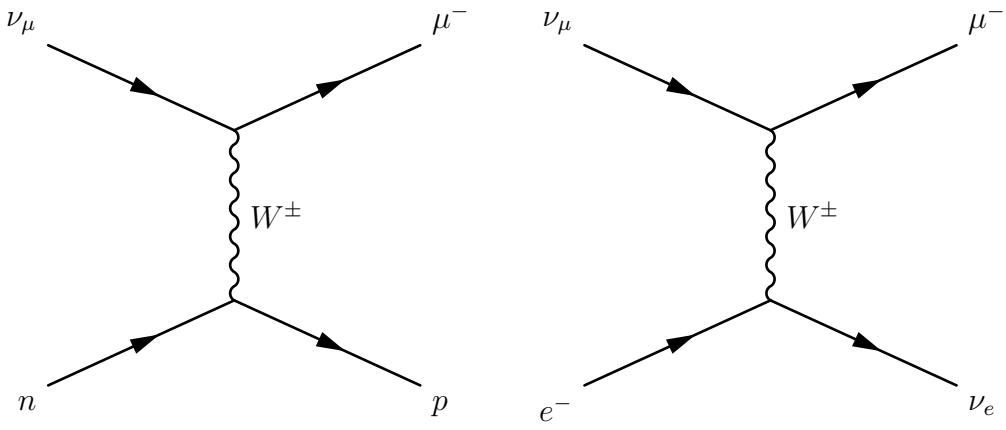

Now it continues its life as a muon that can reach our test setup from below. Within 22 hours of data collection, 20 events can be assigned to an upwards flying particle with hits in all 6 stations. This gives an angular acceptance of $\pm 42\,^\circ$ relative to the z-axis. With the given geometry of the setup, an estimation of the flux can be calculated and compared to measured data of other experiments. 20 events in the given time correspond to a flux of $1,67 \times 10^{-7}\,\mathrm{cm}^{-2}\,\mathrm{s}^{-1}\,\mathrm{sr}^{-1}$. Contrary to this, other experiments

measured orders of magnitude less. Super-Kamiokande declares a flux of $(1,76 \pm 0,1) \times 10^{-13}\,\text{muons}\,\text{cm}^{-2}\,\text{s}^{-1}\,\text{sr}^{-1}$ [5] that come from below with the requirement of entering as well as exiting the detector. Even though the muons that are stopped inside are not considered, this discrepancy is a factor of 10^6. However, other experiments with lower energy thresholds measured fluxes in the same order of magnitude [6]. Combining their measurements with our geometry would lead to one neutrino induced track every 118 years. With such a small expected rate, one has to look for other explanations as neutrino-originating events only make a negligible contribution to the total measured flux from below.

The Extreme Energy Events project, located in Italy published a paper about similar observations in their measurements in 2016 [7]. Their research is focused on the decay of muons.

A muon that is decelerated to almost at rest under the setup will decay after some time. One of the decay products is an electron, which could potentially fly upwards through all of the stations with a highly relativistic maximum energy of 50 MeV. The total material budget of the entire stack is predominated by the thickness of the glass inside each MRPC and the aluminium covers of each detector's housing box. All glass plates add up to almost 3 cm. All 6 aluminium covers make up a total of 6 mm material. Glass, made up of mostly silicon and oxygen has roughly the same density as aluminium ($2,5\,\text{g/cm}^3$ and $2,7\,\text{g/cm}^3$). To simplify the estimation, a total material budget of 3,6 cm aluminium has to be traversed. If one considers all other minor contributing materials, a total of 5 cm would be an exaggeration. The Bethe-Bloch formula is then used to calculate the mean range of electrons at given initial energies. The ESTAR program [8] of the NIST[1] is used for the range estimation. For 50 MeV electrons in aluminium, the CSDA[2] range is roughly 8 cm. A lower limit for the energy with 5 cm range is therefore between 25 - 30 MeV. Accordingly, the physical conditions allow such electrons to be observed. For the purpose of verifying this hypothesis, a closer look to the negative beta events was taken. Upwards moving electrons resulting from downward moving muons

[1] National Institute of Standards and Technology [2] Continuous slowing down approximation

should lead to a time correlation of both signals. Figure 5.23 therefore shows a histogram that contains the information of velocity in units of speed of light and time difference to the previous track (PTD) in ns for every reconstructed track with multiplicity greater than or equal to 5. The most noticeable property is the formation of 4 separated regions. The upper right region dominates the statistics, centered around the speed of light and a PTD of 1/10 th seconds. The average particle rate of the measurement was ∼3 Hz, what matches the observed mean time differences. These are presumably atmospheric muon tracks. Below that, in the lower right are tracks that basically came simultaneous with PTD's around 100 ps.

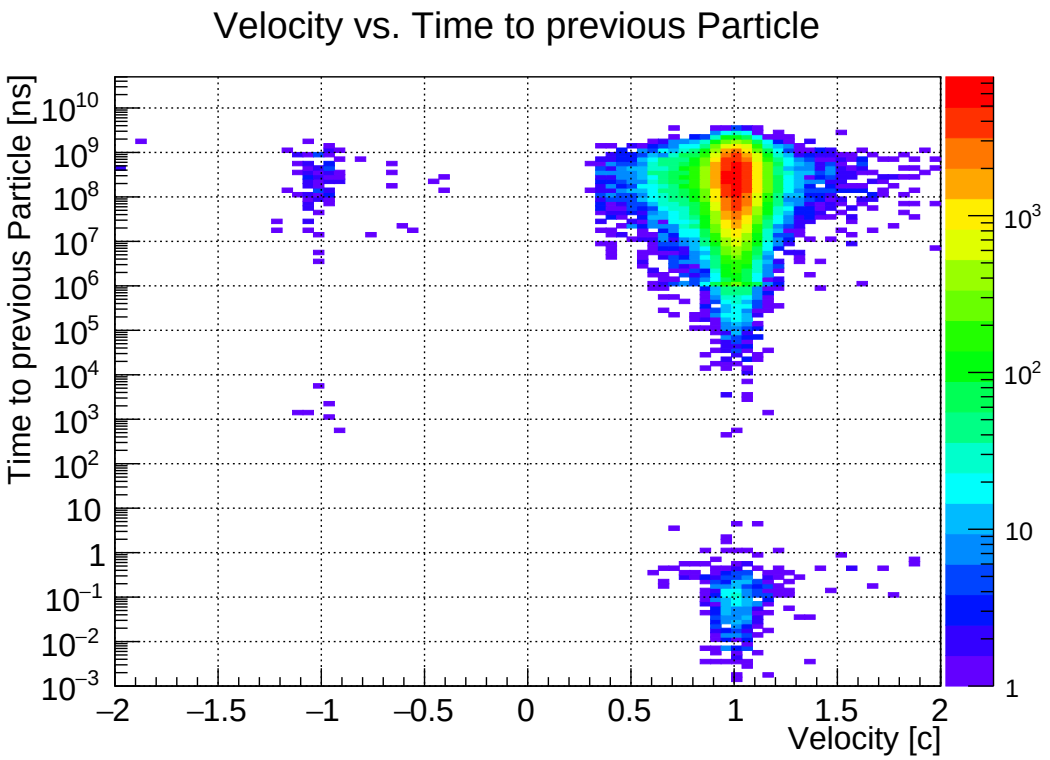

Figure 5.23: A 2D histogram with the particles velocity in units of speed of light on the x-axis and the logarithmic time to the previously arrived track in ns on the y-axis. It can be divided into four areas that start to stand out and make it possible to identify the source.

Simultaneous events belong most probably to hadronic showers in the vicinity above our setup leading to multiple particles entering at the same time.
What is suspected to be electrons can be found on the left hand side of the histogram. Especially interesting is the lower left region with 6 entries. They all appear to come around a few μs after another particle. The muons mean lifetime of about $2\,\mu$s fits to the data quite well. It is feasible to say that the original muon was measured (upper right region) and subsequently decayed on the μs scale afterwards. The resulting electron could then fly upwards again and make it through the stations. The majority of negative velocity tracks follows the PTD of down going muons. These cases are most likely electrons from decaying muons that missed the detectors due to inclination. We find 94 such events and 100 in total that come from below. This results in a probability of $(6,0 \pm 2,5)\,\%$ that the mother particle is detected as well. According to the EEE project [7], they found the mother muon of the up going electrons in 6 % of the cases. The uncertainty is rather large owing to lack of statistics but agrees with what was measured before. Furthermore, most of the negative velocity tracks are only reconstructed if the acceptance is chosen rather large. The fact that electrons are more likely to scatter through coulomb interaction makes their paths more blurred out compared to muons. A reconstruction acceptance that is calibrated on muons is therefore inevitably going to reject those. All together, the data strongly speaks for the hypothesis that the particles from below are indeed electrons originating from (almost) stopped cosmic muons.
With such an example it was shown that the display helps in understanding not only physics inside the detector but also leads to observation of physical processes from the outside. In this special case one even was able to do particle identification to some degree. It can help to better understand the analysing software, too. One finds events with e.g. extraordinarily high cluster sizes, high hit multiplicity where the computer reaches its limit in reconstructing reasonable tracks or time anomalies like afterpulses 5 - 20 ns after an initial hit. In most of the events where a detector is labeled inefficient, the data is present but the matching was done in a wrong way, which is easily judged by eye using the event display.

Chapter 6

Summary and Outlook

For MRPC prototype testing and detector response measurements, a test setup using cosmic muon radiation was built. The electronic components used, were designed and constructed specifically for precise time measurements that are essential when building a TOF system. The investigated two types of MRPCs were built with low resistive glass and soda-lime float glass as resistive material respectively. These types are intended to be used in the intermediate and low rate region of the CBM TOF wall. With a stack of 2 low resistive glass and 4 float glass based detectors observables like efficiency, time & spatial resolutions, cluster size, noise rate, etc. were measured with a tracking approach. The aspired performance goal was reached within these studies. With measured efficiencies of 95-98 % and time resolutions in the order of 50 ps an acceptable performance was proven. Spatial resolutions in x- and y-direction proved to be suitable for track matching with resolutions of 2 mm and 3 mm respectively. Additionally, the low resistive glass based detector showed noise rates, which are high in a cosmic ray environment but negligible compared to the intended irradiation rates. The microscopically rough surface of the low resistive glass is believed to be responsible for the high noise rate. Potential new techniques of casting thin layers of glass instead of polishing it might eliminate the detector noise. Detectors that are physically positioned in the middle of the experimental setup perform worse than equally built ones positioned at each end. Data from previous simulations showed the same results and con-

firm this behaviour. This is explainable by the tracking algorithm being not optimized to perfectly handle cosmic muons without fixed interaction point.
To see possible dependencies of the measured observables from the track's inclination relative to the detector surface, a complete set of measurements were presented. According to the results, highly inclined tracks show no disadvantage in resolving capabilities compared to tracks perpendicular to the surface. Spacial differential analysis, which tracking made feasible, was performed and gave insight into the sensitivity of the measurement. An error during the detector mounting led to a small displacement in the geometry that manifested in reduced performance. It is remarkable how precise one can measure, with the statistics of a few hundred thousand events, even small deviations in the data as shown in the angular and differential analysis. Such high precisions make the results even more convincing and credible. What included a physical application into the measurement were particles with a negative velocity due to an upward movement through the setup from below. Initially assumed rare neutrino induced events were excluded. Publications from the Super-Kamiokande detector suggest only one event in 118 years. From muon decay originating electrons are the more realistic cause and match well with the data. Although with little statistic, 6 % of these upward moving events appeared a few μs after downward moving events. The lifetime of a muon is about 2 μs long and supported the hypothesis of decaying muons. In the case of the other 94 %, the original muon missed the setup due to geometrical constraints.
So far the data readout utilized data transmission via copper cables from the detectors to the AFCK for each channel. The recent implementation of a GBTX[1] board directly attached to the Get4 board reduced the vast amount of copper cables needed to a single optical fiber. Optical fibers are needed in big experiments to cover the large distances to the subsequent electronics where copper cables are not suitable anymore. Whether this impacts the performance in any way is subject to further research. The conditions under which the detectors worked in the laboratory are also different from the ones in the CBM experiment. The mCBM[2] experiment addresses both of these problems.

[1] Giga Bit Transceiver [2] miniCBM

Providing the new readout electronics and an environment with high particle rate, it is planned to test whether the detectors can maintain their level of performance. If this is the case then the outer region of the TOF wall looks promising.

Appendix A

Differential Analysis Histograms

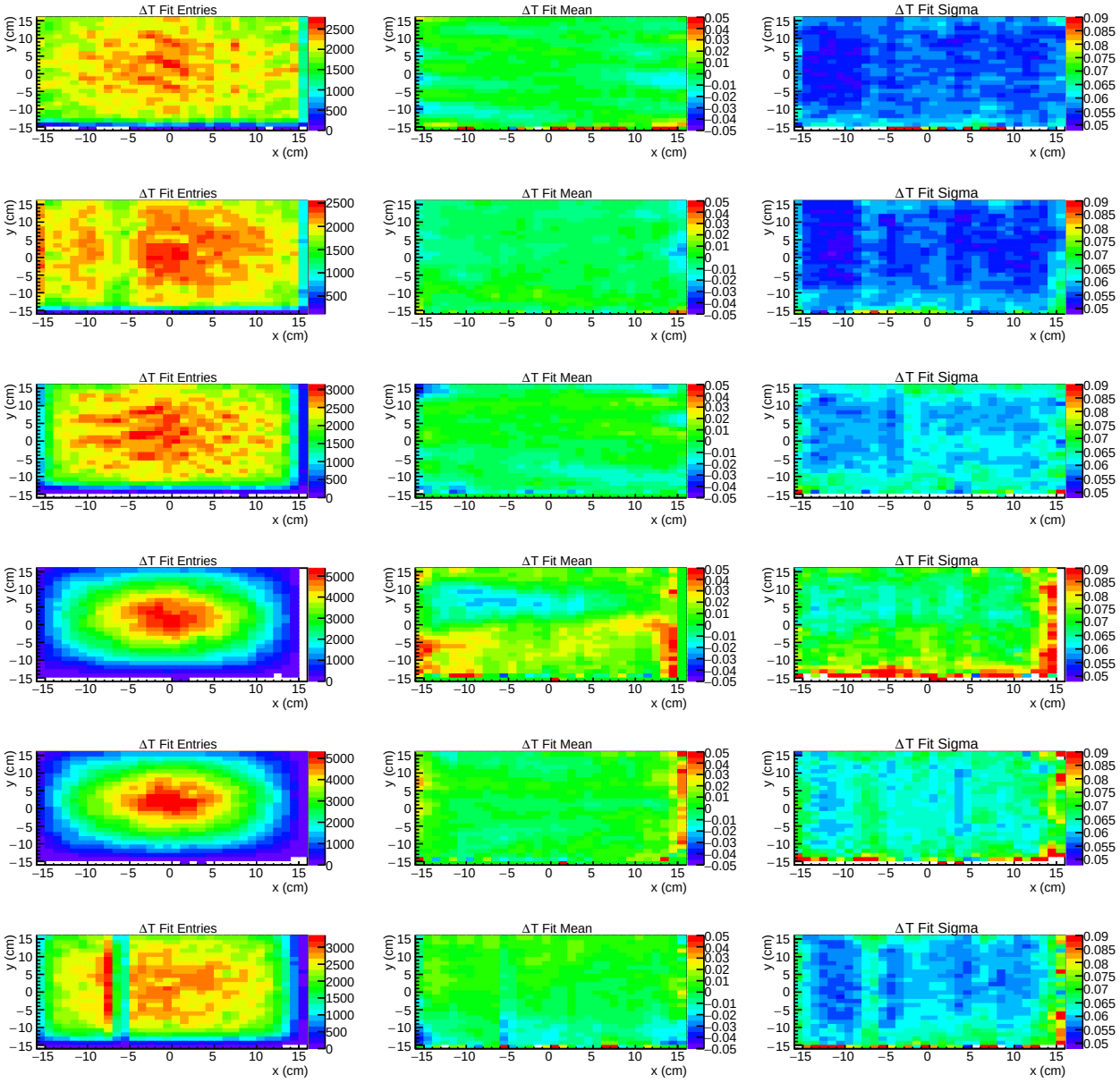

(a) Time measurement differential plots

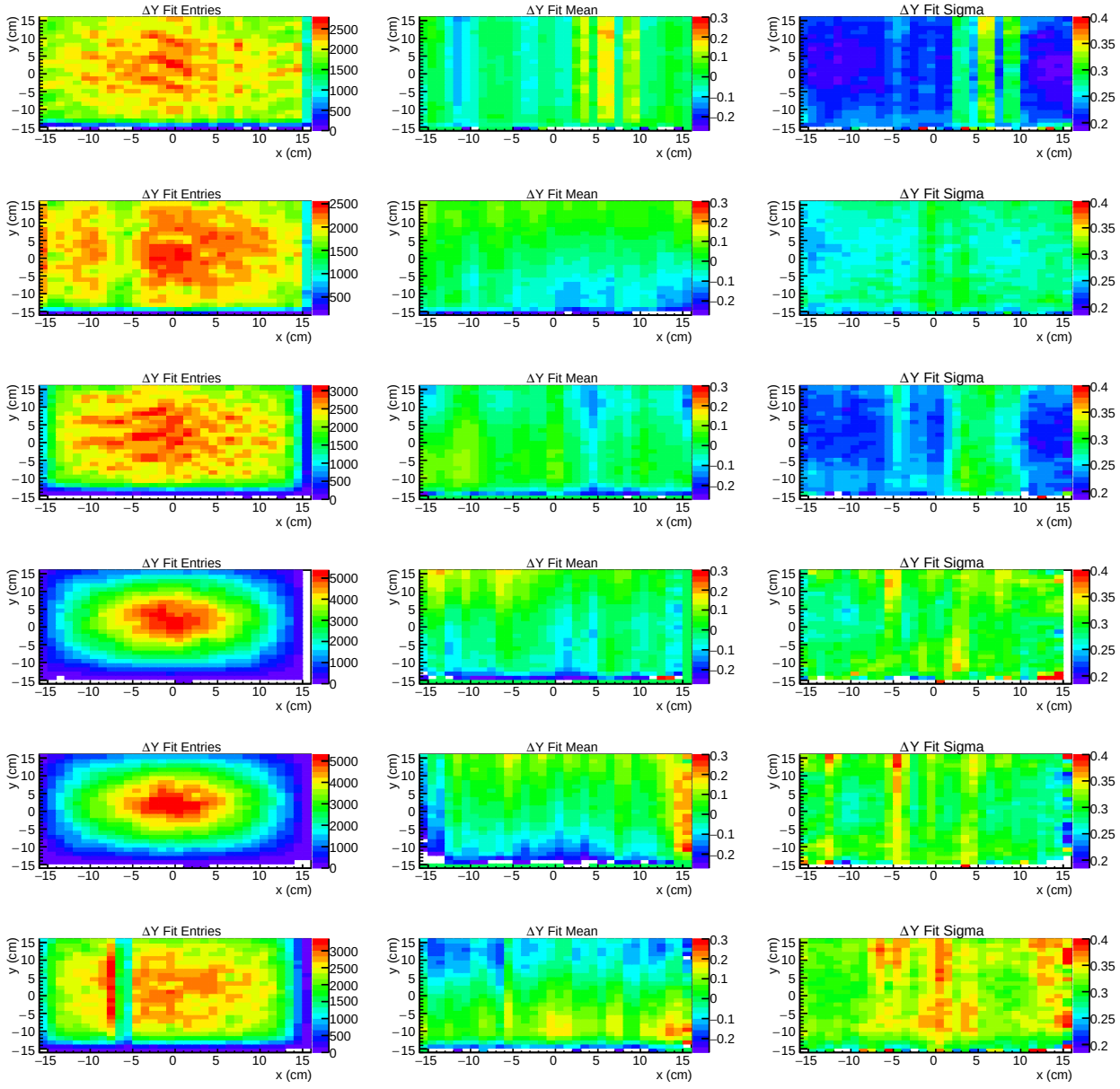

(b) Y measurement differential plots

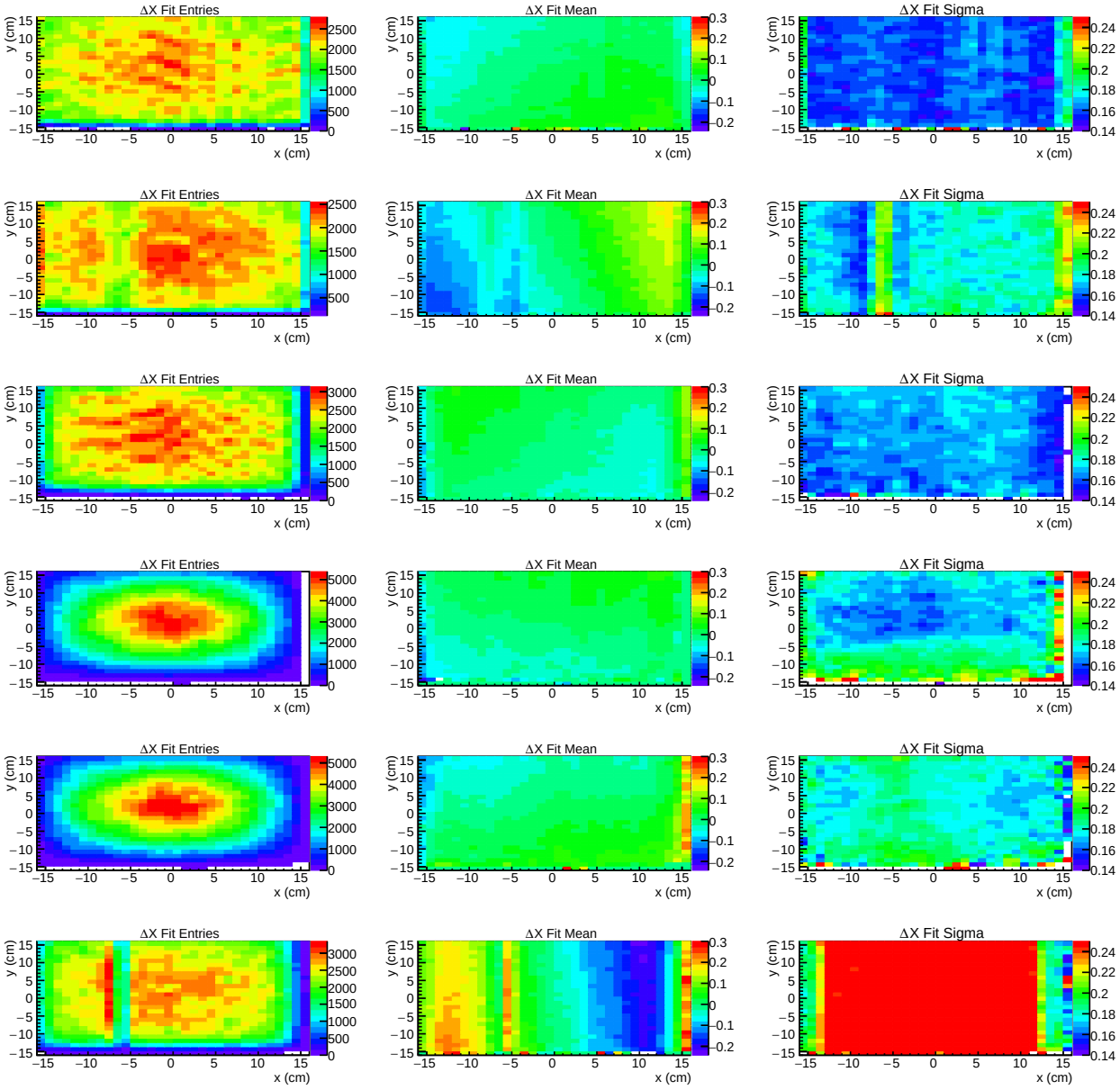

(c) X measurement differential plots

Figure A.1: From top to bottom it is station 0 to station 5 (900, 921, 901, 910, 911, 920). Left column shows the hit distribution, the middle shows the respective residual's mean and the right shows the residuals width.

Bibliography

[1] "CBM Progress Report 2017," Tech. Rep. CBM Progress Report 2017, Darmstadt, 2018.

[2] Y. Wang and Q. Zhang, "Production and Test of MRPC3a," Sept. 2018.

[3] P. Weidenkaff, "Simulation and Software Verification of CBM-ToF Cosmic Data." `https://indico.gsi.de/event/5862/session/18/contribution/132/material/slides/0.pdf`, Mar. 2017.

[4] J. Brandt, "Development of an Event Display for the CBM-ToF Cosmic Test-stand in Heidelberg," Sept. 2018. Bachelorthesis.

[5] The Super-Kamiokande Collaboration and p. b. J. G. Learned, "Underground Muons in Super-KAMIOKANDE," *ArXiv Astrophysics e-prints*, May 1997.

[6] Particle Data Group, "Cosmic Rays." `http://pdg.lbl.gov/2011/reviews/rpp2011-rev-cosmic-rays.pdf`, Aug. 2011. Table 24.3.

[7] M. Abbrescia *et al.*, "A study of upward going particles with the Extreme Energy Events telescopes," 2016.

[8] M. Berger, J. Coursey, M. Zucker, and J. Chang, "Stopping-Power & Range Tables for Electrons, Protons, and Helium Ions." `https://www.nist.gov/pml/stopping-power-range-tables-electrons-protons-and-helium-ions`, July 2017.

Ich versichere, dass ich diese Arbeit selbstständig verfasst und keine anderen als die angegebenen Quellen und Hilfsmittel benutzt habe.

Heidelberg, den 21.12.2018

.....

(Dennis Sauter)